Neuron

Article

Mechanosensitive brain tumor cells construct blood-tumor barrier to mask chemosensitivity

Graphical abstract

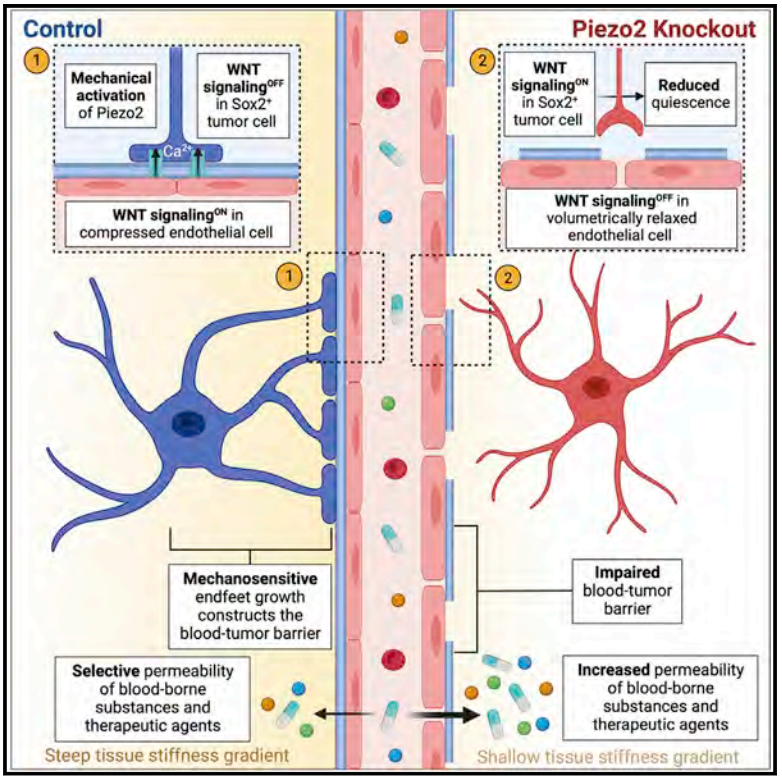

Highlights

- Tumor cells ensheathe capillaries to construct the BTB
- BTB-constructing tumor cells respond to mechanical cues
- Piezo2 governs WNT/β-catenin signaling in tumor and endothelial cells in the BTB
- Piezo2 knockout disrupts BTB and tumor quiescence to elevate chemosensitivity

Authors

Xin Chen, Ali Momin, Siyi Wanggou, ..., Yu Sun, Xuejun Li, Xi Huang

Correspondence

lxjneuro@csu.edu.cn (X.L.), xi.huang@sickkids.ca (X.H.)

In brief

Blood-tumor barrier (BTB) and tumor cell quiescence are two major obstacles in brain cancer treatment. Chen, Momin, and Wanggou et al. show that mechanosensitive tumor cells construct the BTB. Targeting Piezo2 perturbs the BTB and decreases tumor cell quiescence to enhance chemosensitivity of medulloblastoma, the most common pediatric brain cancer.

Chen et al., 2023, Neuron *111*, 30–48
January 4, 2023
https://doi.org/10.1016/j.neuron.2022.10.007

CellPress

CellPress

Neuron

Article

Mechanosensitive brain tumor cells construct blood-tumor barrier to mask chemosensitivity

Xin Chen,[1,2,12] Ali Momin,[1,2,3,12] Siyi Wanggou,[1,2,4,5,12] Xian Wang,[1,2] Hyun-Kee Min,[1,2,3] Wenkun Dou,[6] Zheyuan Gong,[6] Jade Chan,[1,2,3] Weifan Dong,[1,2,3] Jerry J. Fan,[1,2,3] Yi Xiong,[1,2,4,5] Kamilia Talipova,[1,2] Hongyu Zhao,[1,2,4,5] Yuki X. Chen,[7] Kelly Veerasammy,[7] Adam Fekete,[8] Sachin A. Kumar,[1,2] Hongwei Liu,[4,5] Qi Yang,[4,5] Joe Eun Son,[1] Zhengchao Dou,[1,3] Malini Hu,[1,2] Parnian Pardis,[1,2] Kyle Juraschka,[1,2] Laura K. Donovan,[1,2] Jiao Zhang,[1,2] Vijay Ramaswamy,[1,2] Hayden J. Selvadurai,[1,2] Peter B. Dirks,[1,2,3] Michael D. Taylor,[1,2,9,10] Lu-Yang Wang,[8,11] Chi-chung Hui,[1,3] Rinat Abzalimov,[7] Ye He,[7] Yu Sun,[6] Xuejun Li,[4,5,*] and Xi Huang[1,2,3,13,*]

[1]Program in Developmental and Stem Cell Biology, The Hospital for Sick Children, Toronto, ON M5G 1X8, Canada
[2]Arthur and Sonia Labatt Brain Tumour Research Centre, The Hospital for Sick Children, Toronto, ON M5G 1X8, Canada
[3]Department of Molecular Genetics, University of Toronto, Toronto, ON M5S 3E1, Canada
[4]Department of Neurosurgery, Xiangya Hospital, Central South University, Changsha, Hunan 410008, China
[5]Hunan International Scientific and Technological Cooperation Base of Brain Tumor Research, Xiangya Hospital, Central South University, Changsha, Hunan 410008, China
[6]Department of Mechanical and Industrial Engineering, University of Toronto, Toronto, ON M5S 3G8, Canada
[7]Advanced Science Research Center at the Graduate Center, City University of New York, New York, NY 10031, USA
[8]Program in Neurosciences and Mental Health, The Hospital for Sick Children, Toronto, ON M5G 1X8, Canada
[9]Department of Surgery, University of Toronto, Toronto, ON M5S 3E1, Canada
[10]Department of Laboratory Medicine and Pathobiology, University of Toronto, Toronto, ON M5S 3E1, Canada
[11]Department of Physiology, University of Toronto, Toronto, ON M5S 1A8, Canada
[12]These authors contributed equally
[13]Lead contact
*Correspondence: lxjneuro@csu.edu.cn (X.L.), xi.huang@sickkids.ca (X.H.)
https://doi.org/10.1016/j.neuron.2022.10.007

SUMMARY

Major obstacles in brain cancer treatment include the blood-tumor barrier (BTB), which limits the access of most therapeutic agents, and quiescent tumor cells, which resist conventional chemotherapy. Here, we show that Sox2$^+$ tumor cells project cellular processes to ensheathe capillaries in mouse medulloblastoma (MB), a process that depends on the mechanosensitive ion channel Piezo2. MB develops a tissue stiffness gradient as a function of distance to capillaries. Sox2$^+$ tumor cells perceive substrate stiffness to sustain local intracellular calcium, actomyosin tension, and adhesion to promote cellular process growth and cell surface sequestration of β-catenin. Piezo2 knockout reverses WNT/β-catenin signaling states between Sox2$^+$ tumor cells and endothelial cells, compromises the BTB, reduces the quiescence of Sox2$^+$ tumor cells, and markedly enhances the MB response to chemotherapy. Our study reveals that mechanosensitive tumor cells construct the BTB to mask tumor chemosensitivity. Targeting Piezo2 addresses the BTB and tumor quiescence properties that underlie treatment failures in brain cancer.

INTRODUCTION

Brain cancer is among the most challenging cancers to treat. In normal brain, the blood-brain barrier (BBB) consists of capillaries covered by astrocytic endfeet and pericytes. These physical ensheathments, together with vascular basement membrane and tight junctions between endothelial cells, prevent the entry of harmful agents while allowing regulated access of nutrients. While invasive tumor cells populate the perivascular space to displace astrocytic endfeet and breach the blood-tumor barrier (BTB) (Griveau et al., 2018; Watkins et al., 2014), glioma stem-like cells, which have been shown to be able to differentiate into endothelial cells (Hu et al., 2016; Ricci-Vitiani et al., 2010; Wang et al., 2010) or pericytes (Cheng et al., 2013; Zhou et al., 2017), contribute to the BTB to regulate tumor growth and therapy response. As such, the BTB restricts brain access to most therapeutic agents (Arvanitis et al., 2020). Brain tumors display extensive intratumoral heterogeneity, including quiescent tumor cells that resist conventional antimitotic therapy and promote tumor recurrence. Medulloblastoma (MB) is the most common malignant pediatric brain tumor. In MB driven by sonic hedgehog signaling (SHH MB, 30% of all MB), quiescent and slow-cycling tumor-propagating cells express Sox2 or Olig2 (Vanner et al., 2014; Zhang et al., 2019a). Genetic lineage tracing studies

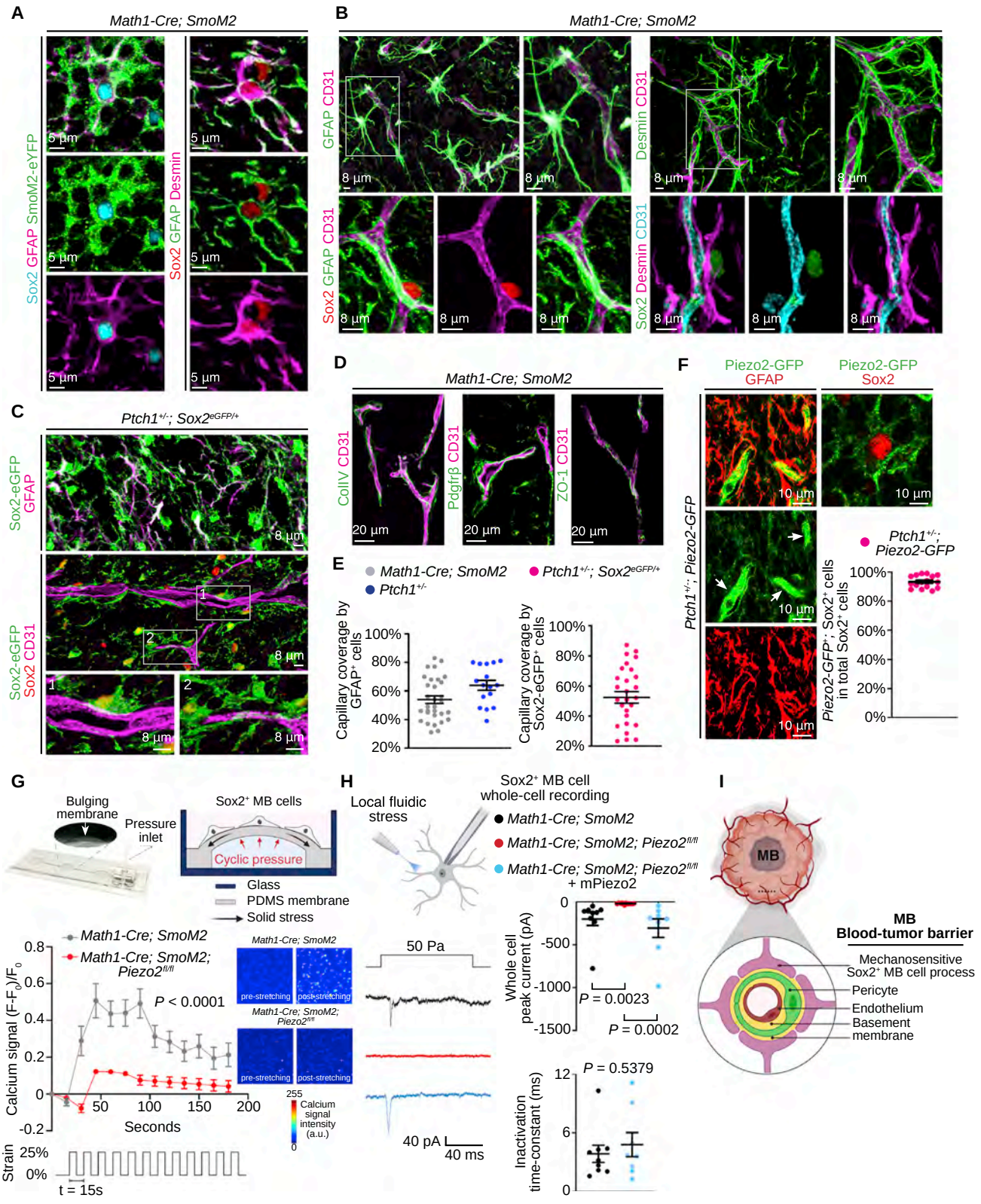

(legend on next page)

showed that despite being a small subset of tumor cells, Sox2$^+$ MB cells give rise to Dcx$^+$ rapidly cycling tumor cells, which differentiate into NeuN$^+$ tumor cells, comprising a Sox2-Dcx-NeuN cellular hierarchy in SHH MB (Vanner et al., 2014). While chemotherapy ablates rapidly cycling tumor cells, Sox2$^+$ cells are chemoresistant and drive post-therapy MB recurrence (Vanner et al., 2014). Due to the BTB and quiescent tumor cells, chemotherapeutic drugs are used at high dosages that result in toxicity yet provide limited benefit (Boyle et al., 2004).

Tumor cells are exposed to microenvironmental mechanical forces (e.g., compression, tension, and shear stress) while tumors develop altered tissue stiffness (Chen and Kumar, 2017; Momin et al., 2021; Northey et al., 2017). Ion channels sense physicochemical cues to regulate ion flux across cell membranes. Piezo mechanosensitive ion channels perceive plasma membrane tension, actomyosin tension, and tissue stiffness to permeate calcium (Murthy et al., 2017), thereby converting mechanical cues into elevations of cytosolic calcium to elicit cell signaling (Jiang et al., 2021). Piezo1 regulates mechanotransduction of nonexcitable cell types in physiological processes such as epithelial homeostasis (Gudipaty et al., 2017) and osteoblast differentiation (Li et al., 2019; Sun et al., 2019). Piezo2 is mainly functional in cells that play mechanosensory roles, such as primary sensory neurons (Ranade et al., 2014b) and touch-sensitive Merkel cells in the skin (Woo et al., 2014). Here, we show that Sox2$^+$ MB cells directly ensheathe capillaries to construct the BTB in a Piezo2-dependent manner. We demonstrate that Piezo2 orchestrates mechano-chemical signaling to govern BTB permeability and Sox2$^+$ MB cell quiescence, revealing an actionable target to elevate chemosensitivity of SHH MB.

RESULTS

Sox2$^+$ MB cells ensheathe tumor capillaries to contribute to the BTB

Activating mutations of *SMO* and inactivating mutations of *PTCH1*, both of which result in aberrant SHH signaling activity, have been identified in human SHH MB (Juraschka and Taylor, 2019; Northcott et al., 2017). To study the BTB in MB, we used *Math1-Cre; SmoM2* mice, in which constitutively active SmoM2 initiates SHH MB from Math1-lineage cells of the cerebellum (Schüller et al., 2008; Yang et al., 2008). MB in *Math1-Cre; SmoM2* mice display characteristic histopathological features and marker expression of human MB (Schüller et al., 2008). We found that Sox2$^+$ MB cells co-express GFAP and Desmin (Figures 1A, S1C, S1D, and S2A). Sox2$^+$, GFAP$^+$, and Desmin$^+$ cells in MB co-express SmoM2-eYFP but not the pericyte marker Pdgfrβ (Figures 1A, S1B–S1D, and S2A), establishing them as neoplastic tumor cells. GFAP expression is unique to Sox2$^+$ cells but not detected in Dcx$^+$ or NeuN$^+$ tumor cells (Figure S1A). Strikingly, Sox2$^+$; GFAP$^+$ and Sox2$^+$; Desmin$^+$ tumor cells project cellular processes (hereafter referred to as endfeet) to directly ensheathe capillaries (Figures 1B, S1B, and S1G). These capillaries are covered by collagen IV$^+$ (ColIV$^+$) basement membrane, Pdgfrβ$^+$ pericytes, and display ZO-1$^+$ tight junctions (Figure 1D), which, together with the ensheathment of Sox2$^+$ MB cells, compose the BTB in MB. We performed lineage tracing using non-MB-bearing *Math1-Cre*; Ai14 mice to determine whether Math1-lineage cells include GFAP$^+$ astrocytes in normal cerebellum. While GFAP$^+$ cells were present in the white matter (WM), internal granule layer (IGL), Purkinje layer (PL), and molecular layer (ML) of the cerebellum of P21 *Math1-Cre*; Ai14 mice, these cells did not express td-Tomato (Figure S1N). These data show that Math1-lineage cells do not include GFAP$^+$ astrocytes in the normal cerebellum, supporting that GFAP$^+$; SmoM2-eYFP$^+$ cells in MB are neoplastic tumor cells, which are formed at an early stage of SHH MB development (i.e., postnatal day 1; Figure S2A).

To confirm that Sox2$^+$ MB cells contribute to the BTB, we genetically labeled Sox2$^+$ cells using the *Sox2$^{eGFP/+}$* reporter (Arnold et al., 2011). As *Ptch1$^{+/-}$* mice develop SHH MB due to the loss of one allele of SHH pathway inhibitor *Ptch1* (Goodrich et al., 1997), we generated *Ptch1$^{+/-}$*; *Sox2$^{eGFP/+}$* mice. *Sox2$^{eGFP/+}$* cells are GFAP$^+$ (Figure S1E) and directly contact capillaries in MB of *Ptch1$^{+/-}$*; *Sox2$^{eGFP/+}$* mice (Figure 1C). Therefore, tumor capillaries were covered by cellular processes extended from Sox2$^+$ MB cells in both *Math1-Cre; SmoM2* and *Ptch1$^{+/-}$* mouse models of SHH MB (Figure 1E). We determined the extent to which Sox2$^+$; GFAP$^+$; SmoM2-YFP$^+$ neoplastic cells cover capillaries, as well as the distribution of fibrinogen, a hepatocyte-secreted protein in blood circulation that only enters brain

Figure 1. Sox2$^+$ MB cells extend endfeet to ensheathe capillaries and are mechanosensitive

(A) Sox2$^+$; GFAP$^+$ cells express SmoM2-eYFP. Sox2$^+$ MB cells express GFAP and Desmin in P21 *Math1-Cre; SmoM2* mice.

(B) Sox2$^+$; GFAP$^+$ and Sox2$^+$; Desmin$^+$ cells extend endfeet to ensheathe CD31$^+$ capillaries.

(C) Sox2-eGFP$^+$ cells express Sox2 and GFAP in *Ptch1$^{+/-}$*; *Sox2$^{eGFP/+}$* MB. Sox2$^+$; Sox2-eGFP$^+$ cells contact and wrap around capillaries.

(D) MB capillaries are covered by ColIV$^+$ basement membrane and Pdgfrβ$^+$ pericytes and display ZO-1$^+$ tight junctions.

(E) Capillaries are ensheathed by Sox2$^+$; GFAP$^+$ MB cells in *Math1-Cre; SmoM2* and *Ptch1$^{+/-}$* MB. Three mice from each group were studied. Each data point represents data from one image. Mean ± SEM.

(F) Piezo2-GFP is expressed in Sox2$^+$ and GFAP$^+$ MB cells. Three mice were studied. Arrows indicate GFAP$^-$; Piezo2-GFP cells. Each data point represents data from one image. Mean ± SEM.

(G) Cell stretching increases calcium signal in Sox2$^+$ cells of *Math1-Cre; SmoM2* MB (n = 15 cells from three P21 mice). Calcium response is decreased in Sox2$^+$ cells of *Math1-Cre; SmoM2; Piezo2$^{fl/fl}$* MB (n = 15 cells from three P21 mice). Representative calcium signals at t = 0 s and t = 30 s are shown. The 3D cell-stretching devices include a PDMS membrane and a chamber to exert cyclic stress on the membrane. Two-way ANOVA; mean ± SEM.

(H) Ejecting a fluidic stream at processes elicits currents at −80 mV from Sox2$^+$ cells of control MB (n = 9 cells from three P21 mice), but not Piezo2 knockout MB (n = 10 cells from three P21 mice). Re-expression of mouse Piezo2 in Sox2$^+$ cells of Piezo2 knockout MB rescues force-evoked whole-cell currents (n = 8 cells from three P21 mice), with inactivation time constant comparable with control Sox2$^+$ MB cells. Kruskal-Wallis test with Dunn's multiple comparisons correction for whole-cell peak current; two-side t test for inactivation time constant; mean ± SEM.

(I) MB BTB consists of mechanosensitive Sox2$^+$ MB cell endfeet, pericyte, vascular basement membrane, and endothelial cell.

See also Figures S1 and S2.

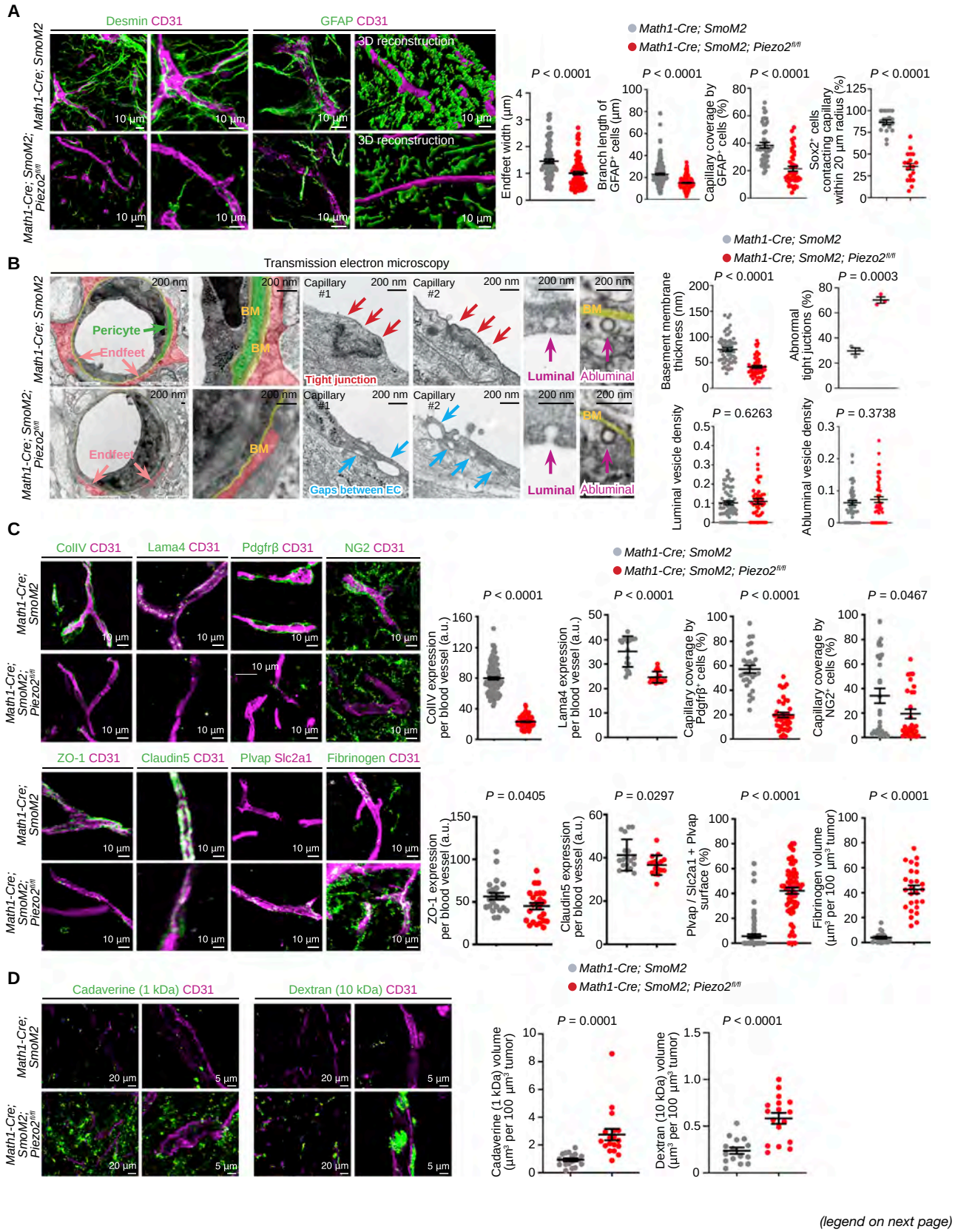

(legend on next page)

parenchyma through a leaky brain barrier, in *Math1-Cre; SmoM2* mice across early to late MB tumorigenesis stages (P0, P7, P11, and P21). Interestingly, as capillary coverage by $Sox2^+$, $GFAP^+$, SmoM2-YFP^+ cells gradually increased, the intratumoral fibrinogen level gradually decreased (Figure S1F). This anticorrelation suggests that BTB construction by $Sox2^+$ MB cells is a time-dependent process. $CD31^+$ or $Pdgfr\beta^+$ cells did not express SmoM2-eYFP (Figures S1C and S1D), showing that no MB cells differentiate into endothelial cells or pericytes. The blood vessel-ensheathing astrocytic endfeet in the cortex and blood vessel-ensheathing $GFAP^+$ cell endfeet in MB expressed AQP4 (Figure S1G). Taken together, these data establish that $Sox2^+$ MB cells ensheathe capillaries in the BTB (Figure 1I).

$Sox2^+$ MB cells are mechanosensitive in a Piezo2-dependent manner

We next asked whether MB cells express mechanosensitive Piezo channels. To determine Piezo expression *in vivo*, we used *Piezo2-GFP-IRES-Cre* and *Piezo1-tdTomato* mice, which report endogenous Piezo2 and Piezo1 expression by GFP (Woo et al., 2014) and tdTomato (Ranade et al., 2014a), respectively. Piezo2 was expressed in $GFAP^+$ and $Sox2^+$ cells, as well as $CD31^+$ endothelial cells and $Pdgfr\beta^+$ pericytes, in MB of *Ptch1*$^{+/-}$*; Piezo2-GFP* mice (Figures 1F and S2B). No overt Piezo2 expression was detected in $Sox2^+$ or $Nestin^+$ cells in the cerebellum (Figure S2C) or $Ki67^+$ proliferative cerebellum granule neuron precursors (Figure S2D), which are putative cells of origin for SHH MB (Schüller et al., 2008; Yang et al., 2008). Both Piezo2 and Piezo1 expressions were detected in endothelial cells and pericytes (Figures S2C–S2F and S2H), while Piezo1 expression was not detected in tumor cells (Figure S2G). $GFAP^+$ astrocytes, which ensheathe capillaries in cortex of *Ptch1*$^{+/-}$*; Piezo2-GFP* mice, displayed Piezo2-GFP (Figure S1H). In contrast, while *Piezo2* expression was detected in the normal brain (Figure S1K), capillary-ensheathing $GFAP^+$ astrocytes did not appear to display Piezo2-GFP (Figure S1I), consistent with a recent report (Chi et al., 2022). These findings suggest that Piezo2-GFP expression in cortical astrocytes could be a consequence of global *Ptch1*$^{+/-}$ heterozygosity or a pathological response of the MB-bearing brain.

We asked whether $Sox2^+$ MB cells can respond to mechanical cues. First, we performed cell stretching and calcium imaging using $Sox2^+$ MB cells isolated from control (*Math1-Cre; SmoM2*) and Piezo2 knockout (*Math1-Cre; SmoM2; Piezo2*$^{fl/fl}$) MB (Figures S3A and S3B). In these mice, *Math1-Cre* driver deleted genes in neoplastic cells but not endothelial cells or pericytes (Figures S1C and S1D). Our cell-stretching device included a chamber connected to a pneumatic pump for exerting cyclic pressure, which bulged a PDMS membrane to apply mechanical stress to cells (Figure 1G). Calcium signals of control $Sox2^+$ MB cells increased, followed by a slow decrease toward the baseline (Figure 1G), likely due to calcium efflux mechanism to prevent calcium toxicity. Piezo2 knockout $Sox2^+$ MB cells displayed decreased calcium response (Figure 1G). Furthermore, we performed patch clamp recording to compare force-evoked whole-cell currents. Locally ejecting a fluidic stream at cellular processes of $Sox2^+$ MB cells activated inward currents, which were abrogated by Piezo2 knockout (Figure 1H). Re-expressing Piezo2 restored force-activated currents in Piezo2 knockout $Sox2^+$ MB cells (Figures 1H and S1J). These data establish $Sox2^+$ cells as mechanosensitive, a property conferred by Piezo2. Piezo2 knockout $Sox2^+$ MB cells still displayed mechanically activated calcium response upon global cell stretching (Figure 1G). Interestingly, Piezo2 knockout $Sox2^+$ MB cells upregulated the expression of *Trpv4*, a putative mechanosensitive ion channel (Figure S1L). Treatment with Gd^{3+}, a broad-spectrum blocker of mechanosensitive ion channels, eliminated mechanically induced calcium signals in both control and Piezo2 knockout $Sox2^+$ MB cells (Figure S1M). These data suggest that other mechanosensitive ion channels, such as *Trpv4*, may contribute to mechanically induced calcium response in the absence of Piezo2. Piezo2 appears to be the principal channel that responds to mechanical stimulation at cellular processes of $Sox2^+$ MB cells (Figure 1I).

Tumor-specific Piezo2 knockout disrupts the BTB

We next investigated the role of Piezo2 in the BTB. Strikingly, the BTB is profoundly altered in Piezo2 knockout MB. First, Piezo2 knockout decreases the length and width of cellular processes but not the number of $Sox2^+$ MB cells. As a result, the extent of capillary coverage is reduced, and the percentage of $Sox2^+$ MB cells that contact capillaries is decreased (Figures 2A, 2B, and S3C). Second, transmission electron microscopy (TEM) reveals vascular basement membrane thinning (Figure 2B). In normal BBB, Laminin $\alpha 2$ (Lama2) is produced by astrocytes and possibly pericytes at the gliovascular interface (Menezes et al., 2014). Laminin $\alpha 4$ (Lama4) is expressed by endothelial cells at the sprouting vascular front (Stenzel et al., 2011). ColIV can be derived from endothelial cells, astrocytes, and pericytes (Baeten and Akassoglou, 2011; Xu et al., 2019). Lama4 and ColIV

Figure 2. Tumor-specific Piezo2 knockout disrupts the BTB

(A) Tumor-specific Piezo2 knockout decreases capillary ensheathment by $GFAP^+$ or $Desmin^+$ cell processes. Three to five P21 mice from each group were studied. Each data point represents data from one cell or structure unit. Two-tailed t test; mean ± SEM.

(B) Transmission electron microscopy shows reduced endfeet ensheathment, pericyte coverage, basement membrane thickness, and disrupted tight junctions but not endothelial cell luminal or abluminal vesicles in Piezo2 knockout MB. Red arrows indicate electron dense tight junctions. Blue arrows indicate endothelial cells with enlarged paracellular space. Magenta arrows indicate luminal and abluminal vesicles in endothelial cells. Three P21 mice from each group were studied. Each data point represents data from one image except tight junction analysis, in which each data point represents one mouse. Two-tailed t test; mean ± SEM.

(C) Immunostaining shows decreased $ColIV^+$ and $Lama4^+$ basement membrane, reduced $Pdgfr\beta^+$ and $Ng2^+$ pericyte coverage, diminished ZO-1^+ and $Claudin5^+$ tight junctions, and ectopic Plvap expression in endothelial cell of Piezo2 knockout MB. Fibrinogen displays increased distribution in perivascular regions of Piezo2 knockout MB. Three P21 mice from each group were studied. Each data point represents data from one image. Two-tailed t test; mean ± SEM.

(D) Cadaverine and dextran dye distribution in MB. Three P21 mice from each group were studied. Each data point represents data from one image. Two-tailed t test; mean ± SEM.

See also Figure S3.

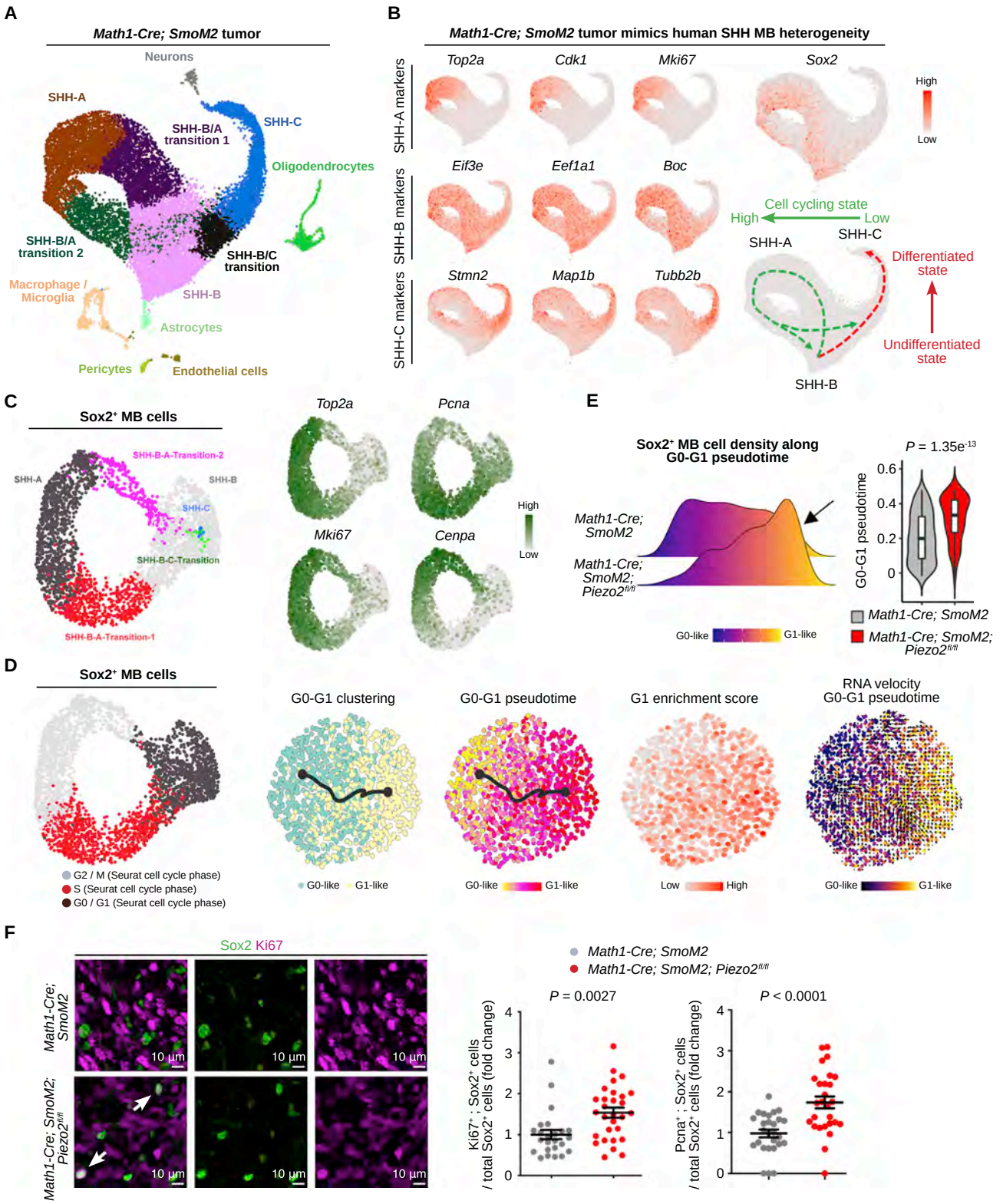

(legend on next page)

expression is decreased (Figures 2C and S3D), while Lama2 expression is increased in Piezo2 knockout MB (Figure S3E). These data collectively demonstrate a markedly perturbed vascular basement membrane structure in the BTB of Piezo2 knockout MB. Third, as Pdgfrβ$^+$ and Ng2$^+$ pericytes cover blood vessels to maintain vascular homeostasis (Armulik et al., 2010; Daneman et al., 2010; Hall et al., 2014), Piezo2 knockout reduces vasculature-associated pericytes (Figures 2B, 2C, and S3D). Fourth, vascular tight junctions, as delineated by TEM, ZO-1, and Claudin5 immunostaining, are disrupted in Piezo2 knockout MB (Figures 2B, 2C, and S3D). Of note, the space between adjoining endothelial cells is substantially widened (arrows in Figure 2B). Fifth, a conspicuous difference is detected in marker expression in endothelial cells. The nonfenestrated blood vessels of central nervous system (CNS) express Slc2a1, while plasmalemma vesicle-associated protein (Plvap) expression marks fenestrated blood vessels in non-CNS sites. In comparison to Slc2a1$^+$; Plvap$^-$ endothelial cells of control MB, endothelial cells of Piezo2 knockout MB display a Slc2a1$^+$; Plvap$^+$ immunophenotype (Figures 2C and S3D). Sixth, deposition of fibrinogen is increased in perivascular regions of Piezo2 knockout MB (Figures 2C and S3D). To corroborate the vascular permeability phenotype, we performed retro-orbital injection of Cadaverine (1 kDa) or Dextran (10 kDa) fluorescent dyes into MB-bearing mice. Piezo2 knockout MB displays elevated intratumoral distribution of Cadaverine and Dextran (Figure 2D). The density of endothelial luminal and abluminal vesicles, "Transcytosis" gene signature, as well as expression of *Mfsd2a* (Ben-Zvi et al., 2014), which are regulators of endothelial transcytosis, are unaffected by Piezo2 knockout (Figures 2B and S3F). Capillary diameter, number, density, cylindricalness, the mitosis or apoptosis of endothelial cells, and P-glycoprotein expression of endothelial cells are also unchanged (Figures S3G and S3H).

Piezo2 knockout decreases the quiescence of Sox2$^+$ MB cells

Having observed profound BTB phenotypes in Piezo2 knockout MB, we performed single-cell RNA sequencing (scRNA-seq) to investigate tumor cell states. We identified neoplastic cells and stromal cell types (Figures 3A and S4A). Of note, we identified altered gene set enrichment analysis (GSEA) signatures in "cell junction assembly," "maintenance of BBB," and "regulation of vascular development" in endothelial cells in Piezo2 knockout MB (Figure S3F), providing further support of the BTB phenotypes. A single-cell transcriptomic study of human SHH MB identified intratumoral heterogeneity with three transcriptional programs, each with a predominant signature in cell cycle activity (SHH-A), undifferentiated state (SHH-B), or differentiated state (SHH-C) (Hovestadt et al., 2019). Tumors in *Math1-Cre; SmoM2* mice mimic these heterogeneous transcriptional programs found in human SHH MB (Figures 3A, 3B, S4A, and S4B). We found two paths through which MB cell states progress among the three transcriptional programs: either along the cell cycling path or the cellular differentiation path (Figures 3B and S4B). Sox2$^+$ MB cells display intratumoral heterogeneity by predominantly distributing to SHH-A and SHH-B clusters (Figures 3B and 3C).

Since tumor cell quiescence, which influences therapeutic outcomes, is a state change between G0 and G1, we focused on comparing Sox2$^+$ MB cells at these two cell cycle states (Figure 3D). We determined cell cycle phases by Seurat and identified G0 and G1 Sox2$^+$ MB cell clusters by uniform manifold approximation and projection (UMAP) analysis (Figure 3D). We reconstructed a linear pseudotime trajectory representing continuous cell states between G0 and G1 clusters (Figure 3D). Differential gene expression gene analysis showed upregulated quiescent markers in the G0-like cluster and downregulated quiescent markers in the G1-like cluster (Figure S4C). We performed G1 gene enrichment analysis and observed that G1-like cells display higher G1 enrichment score (Figures 3D and S4C). Piezo2 knockout increases the density of G1-like Sox2$^+$ MB cells along pseudotime (Figure 3E), suggesting that Piezo2 knockout decreases the quiescence of Sox2$^+$ MB cells.

Next, we performed immunostaining experiments to corroborate the cell cycle phenotype revealed by scRNA-seq. While most neoplastic cells are cycling in MB (Figure S4D), the fraction of Ki67$^+$; Sox2$^+$ cells (cycling Sox2$^+$ cells) within total Sox2$^+$ cells is increased in Piezo2 knockout tumors (Figure 3F). Furthermore, using Pcna as another marker for cycling cells, we found that the fraction of Pcna$^+$; Sox2$^+$ cells within total Sox2$^+$ cells is also increased in Piezo2 knockout MB (Figure 3F). Collectively, these data not only demonstrate the heterogeneity of Sox2$^+$ MB cells, which include both quiescent and cell cycling fractions, but also show that Piezo2 knockout decreases the quiescence of Sox2$^+$ MB cells.

Targeting Piezo2 enhances MB chemosensitivity

Next, we investigated the impact of Piezo2 knockout on therapy-naive and chemotherapy-treated MB. Tumor-specific Piezo2 knockout did not alter the overall number of mitotic tumor cells,

Figure 3. Piezo2 regulates the quiescence of Sox2$^+$ MB cells

(A) scRNA-seq identifies neoplastic cells and stromal cell types in SHH MB of P21 mice.

(B) Cell type clustering analysis shows three transcriptional programs (SHH-A, SHH-B, SHH-C) and two routes (green and red dotted lines) for cell state transitioning.

(C) Sox2$^+$ MB cells display intratumoral heterogeneity by predominantly distributing to SHH-B and SHH-A cell clusters. Cell cycle genes, such as *Top2a*, *Pcna*, *Mki67*, and *Cenpa*, display heterogeneous expression in Sox2$^+$ MB cells.

(D) UMAP analysis identifies G0-like and G1-like Sox2$^+$ MB cells. Pseudotime analysis shows cell state progression between two clusters. G1-like Sox2$^+$ MB cells display higher G1 enrichment score.

(E) Piezo2 knockout elevates the density of G1-like Sox2$^+$ MB cells in pseudotime. Three mice from each group were studied.

(F) The fraction of Ki67$^+$; Sox2$^+$ cells or Pcna$^+$; Sox2$^+$ cells within total Sox2$^+$ cells is elevated by Piezo2 knockout. Five P21 mice from each group were studied for Ki67$^+$; Sox2$^+$ quantification. Three P21 mice from each group were studied for Pcna$^+$; Sox2$^+$ quantification. Each data point represents data from one image. Two-tailed t test; mean ± SEM.

See also Figure S4.

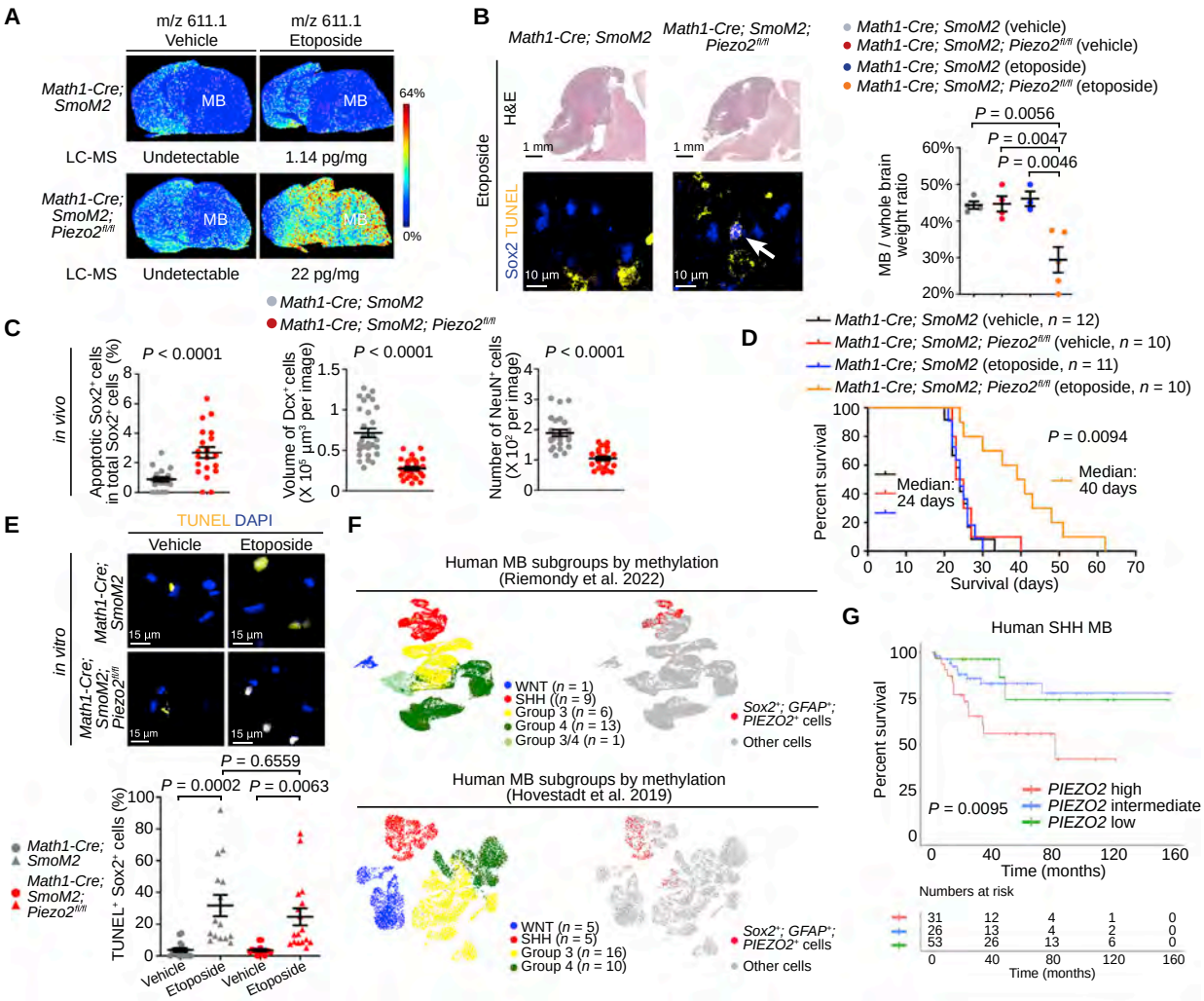

(legend on next page)

the apoptosis of Sox2$^+$ MB cells, or mouse survival under therapy-naive conditions (Figures S5A–S5C). Etoposide, which forms a complex with topoisomerase II to inhibit DNA synthesis and cell cycle progression, entered the brain to a limited extent (Zhou et al., 2017). To interrogate BTB's ability to ward off chemotherapeutic agents, we examined MB-bearing mouse brains after intraperitoneal etoposide injection. We performed matrix-assisted laser desorption/ionization (MALDI) imaging mass spectrometry (MS), which provides spatial information of molecules with a specific molecular mass, and liquid chromatography-MS (LC-MS), which identifies molecules of interest. Strikingly, we detected more than 19-fold increase of etoposide in *Math1-Cre; SmoM2; Piezo2$^{fl/fl}$* MB compared with control 2 h post intraperitoneal injection (Figure 4A). Five daily etoposide treatments dramatically reduced tumor burden and Dcx$^+$ and NeuN$^+$ tumor cells in *Math1-Cre; SmoM2; Piezo2$^{fl/fl}$* mice (Figures 4B and 4C). Importantly, the etoposide treatment increased apoptosis in Sox2$^+$ MB cells (Figures 4B and 4C) and extended the survival of *Math1-Cre; SmoM2; Piezo2$^{fl/fl}$* mice (Figure 4D). In stark contrast, no survival benefit was detected in etoposide-treated *Math1-Cre; SmoM2* mice compared with vehicle-treated mice of either genotype (Figure 4D). We treated cultured Sox2$^+$ MB cells derived from control and Piezo2 knockout tumors. While Sox2$^+$ MB cells displayed an elevated apoptotic response to etoposide treatment *in vivo*, control and Piezo2 knockout MB Sox2$^+$ cells displayed comparable apoptotic responses *in vitro* (Figure 4E). The *in vitro* culture condition promoted rapid cell cycling of Sox2$^+$ MB cells (Vanner et al., 2014). As such, the difference in cell cycling between control and Piezo2 knockout Sox2$^+$ MB cells observed *in vivo* was absent when these cells were cultured *in vitro* (Figure S5D). These data suggest that *in vivo* reduction of Sox2$^+$ MB cell quiescence is a cell nonautonomous consequence likely associated with the compromised BTB in Piezo2 knockout MB. Interestingly, etoposide was seen in brain tissue adjacent to MB (Figure 4A). In agreement, we detected elevated levels of Cadaverine in nontumoral brain tissue of mice bearing Piezo2 knockout MB (Figure S5E). We postulate that etoposide and Cadaverine entered through the disrupted BTB in MB and were subsequently distributed to wider brain regions.

PIEZO2 is expressed in human SHH MB and regulates BTB permeability

To investigate the human relevance of our findings from mice, we analyzed two scRNA-seq datasets of human MB, both of which include all four MB subgroups (Hovestadt et al., 2019; Riemondy et al., 2022). In both datasets, *PIEZO2$^+$; SOX2$^+$; GFAP$^+$* MB cells were readily identified. *PIEZO2$^+$; SOX2$^+$; GFAP$^+$* cells were selectively present in human SHH MB in the Riemondy et al. dataset, while *PIEZO2$^+$; SOX2$^+$; GFAP$^+$* cells were predominantly present in human SHH MB and less frequently in other MB subgroups in the Hovestadt et al. dataset (Figure 4F). Interestingly, *PIEZO1* expression was prominent in groups 3 and 4 MB (Figure S5F). High *PIEZO2* expression was associated with worse survival of patients with SHH, but not WNT, groups 3 or 4 MB (Figures 4G, S6A, and S6B). Notably, this association was also detected when SHH MB patients under the age of 17 years, who all had undergone chemotherapy treatment, were analyzed (Figure 4G). We performed orthotopic xenograft using ONS76 (a human SHH MB cell line) and SHH-MB-1 (a SHH MB patient-derived line). In both xenograft tumors, human MB cells (labeled by human-specific antigen STEM121; Figure S6C) that are in direct contact with capillaries are detected (Figures 4H and S6D). Xenograft tumors derived from ONS76 cells with PIEZO2 knockdown showed decreased tumor cell coverage on capillaries, reduced vascular basement membrane thickness, and increased paracellular space between endothelial cells (Figure 4H). We performed retro-orbital injection of Evans blue dye to assess vascular permeability in mice bearing control and PIEZO2 knockdown xenograft tumors. PIEZO2 knockdown profoundly increased Evans blue dye distribution in xenograft

Figure 4. Piezo2 knockout unmasks therapeutic vulnerability of MB

(A) MALDI imaging mass spectrometry and LC-MS to identify etoposide in brains of P21 mice intraperitoneally injected with vehicle or etoposide. MALDI imaging mass spectrometry signal in vehicle-treated brains is from tissue-endogenous molecule(s) at the same molecular weight as etoposide. Etoposide concentrations are determined by LC-MS.

(B) Etoposide treatment effect on tumor burden and apoptosis of Sox2$^+$ MB cells. For tumor weight comparison: control mice treated with vehicle (n = 4) and etoposide (n = 3) and Piezo2 knockout mice treated with vehicle (n = 4) and etoposide (n = 5) were studied. One-way ANOVA with Tukey's multiple comparisons correction; mean ± SEM.

(C) Etoposide treatment effect on apoptosis of Sox2$^+$ MB cells, volume of Dcx$^+$ cells, and number of NeuN$^+$ cells. Three mice from each group were studied. Each data point represents data from one image. Two-tailed t test; mean ± SEM.

(D) Etoposide treatment extends the survival of Piezo2 knockout mice. Etoposide treatment provides no benefit to control mice in comparison with vehicle-treated mice of either genotype. Control mice treated with vehicle (n = 12) and etoposide (n = 11) and Piezo2 knockout mice treated with vehicle (n = 10) and etoposide (n = 10) were studied. Kaplan-Meier survival curve was analyzed using log-rank test.

(E) Apoptotic response to etoposide of control and Piezo2 knockout Sox2$^+$ MB cells *in vitro*. Cells from three mice were studied in each group. Each data point represents data from one image. One-way ANOVA with Tukey's multiple comparisons correction; mean ± SEM.

(F) *PIEZO2$^+$; SOX2$^+$; GFAP$^+$* MB cells are identified in two scRNA-seq datasets of human MB.

(G) High *PIEZO2* expression associates with worse survival of SHH MB patients under the age of 17 years. Kaplan-Meier survival curve was analyzed using log-rank test.

(H) PIEZO2 knockdown decreases human tumor cell coverage on capillaries, reduces vascular basement membrane thickness, and increases paracellular space between endothelial cells in ONS76 xenograft tumors. Three mice from each group were studied for quantification. Each data point represents data from one image. One-way ANOVA with Tukey's multiple comparisons correction; mean ± SEM.

(I) PIEZO2 knockdown increases distribution of Evans blue dye in ONS76 xenograft tumors and the apoptotic response of tumor cells after etoposide treatment. Three mice from each group were studied. Each data point represents data from one image. One-way ANOVA with Tukey's multiple comparisons correction; mean ± SEM.

See also Figures S5 and S6.

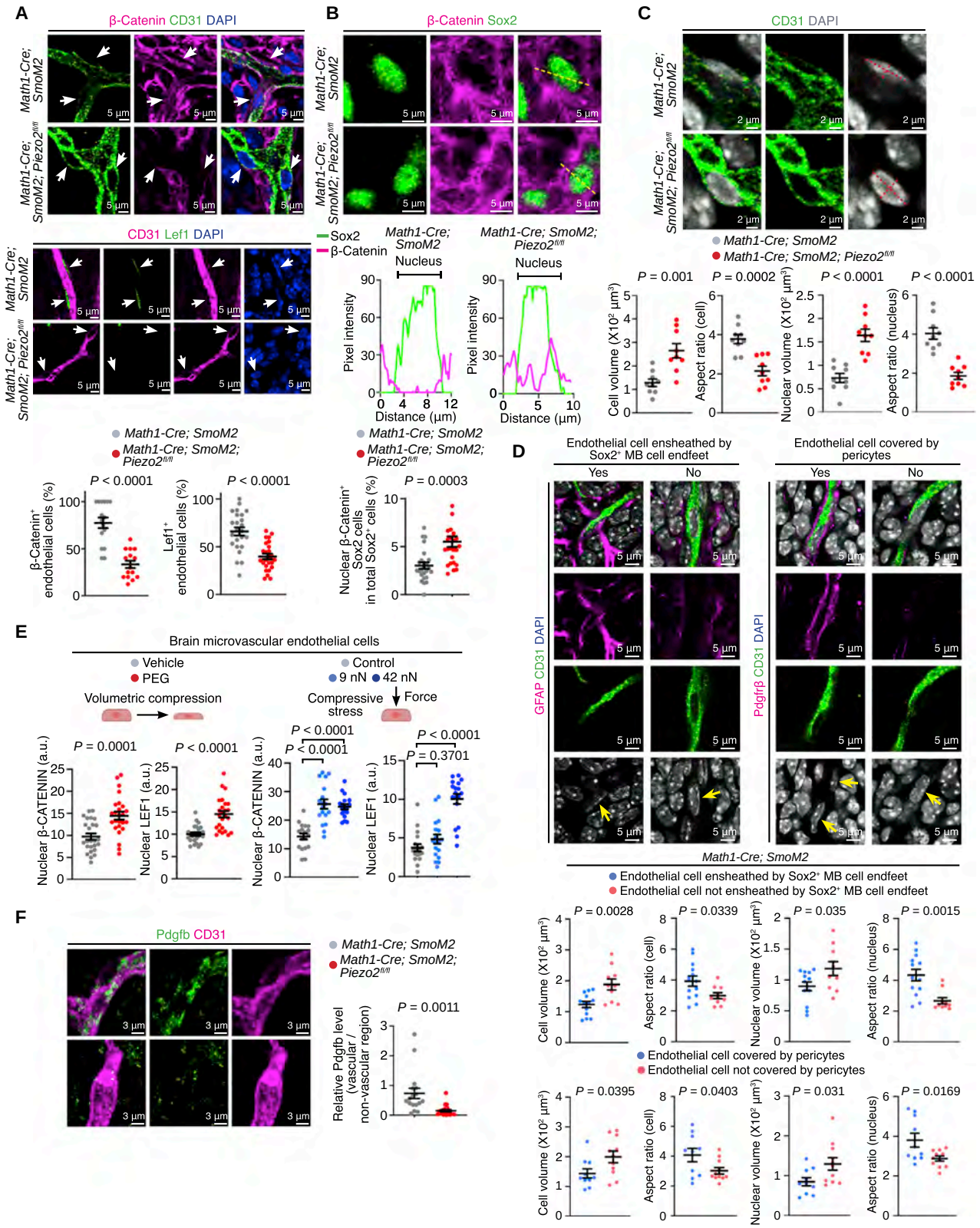

(legend on next page)

tumors (Figure 4I). Furthermore, we treated xenograft tumor-bearing mice with vehicle or etoposide. Tumor cells displayed comparable apoptosis between vehicle-treated mice bearing control and PIEZO2 knockdown tumors. In contrast, etoposide treatment elevated apoptosis in PIEZO2 knockdown tumors compared with control (Figure 4I). Collectively, the identification of *PIEZO2*$^+$*; SOX2*$^+$*; GFAP*$^+$ tumor cells predominantly in human SHH MB, the association between high *PIEZO2* expression and worse survival of SHH MB patients, and the BTB and chemosensitivity phenotypes in xenograft tumors support a role of PIEZO2 in human MB.

Piezo2 governs WNT/β-catenin signaling in Sox2$^+$ MB cells and endothelial cells

Next, we investigated the mechanism by which Piezo2 regulates the BTB and Sox2$^+$ MB cells. In the normal brain, WNT/β-catenin signaling in endothelial cells is required for the formation of BBB and its barrier properties (Arvanitis et al., 2020; Langen et al., 2019; Sweeney et al., 2019). Tumor cells in MB driven by constitutive WNT signaling (WNT MB) secrete WNT antagonists to suppress WNT/β-catenin signaling in endothelial cells, resulting in a compromised brain barrier and greater chemotherapeutic response compared with SHH MB (Phoenix et al., 2016). Our scRNA-seq data show that SHH MB harbors a microenvironment with Wnt ligand expression (Figure S6E). Indeed, we detected nuclear β-catenin and Lef1, both of which indicate active WNT/β-catenin signaling, in endothelial cells of control MB (Figure 5A). Strikingly, WNT/β-catenin signaling is reduced in endothelial cells of Piezo2 knockout MB (Figure 5A). To interrogate Wnt/β-catenin signaling in Sox2$^+$ MB cells, we performed three comparisons. First, we compared nuclear β-catenin levels based on immunostaining. Second, we compared the expression of *Axin2*, a readout for Wnt/β-catenin signaling, as well as "Hallmark of WNT/β-catenin signaling" gene expression enrichment score based on scRNA-seq. Third, we performed Lef1 immunostaining. We consistently detected increased nuclear β-catenin signals (Figure 5B), increased *Axin2* expression (Figure S6F), and elevated Hallmark of WNT/β-catenin signaling gene expression enrichment score (Figure S6F) in Piezo2 knockout Sox2$^+$ MB cells. We did not detect overt Lef1 immunostaining signal in either control or Piezo2 knockout Sox2$^+$ MB cells. β-catenin nuclear import can occur independently of LEF/TCF transcription factor binding (Fagotto et al., 1998; Prieve and Waterman, 1999). TCF/LEF-dependent and -independent regulation of nuclear β-catenin activity governs distinct subsets of WNT transcriptional targets (Doumpas et al., 2019). We postulate that activation of WNT/β-catenin signaling may engage Lef1-independent downstream mechanisms in Piezo2 knockout Sox2$^+$ MB cells. Our data suggest that Piezo2 knockout leads to a modest increase of Wnt/β-catenin signaling in Sox2$^+$ MB cells without inducing overt Lef1 expression detectable by immunostaining. Taken together, Piezo2 governs WNT/β-catenin signaling in endothelial cells and Sox2$^+$ MB cells.

Volumetric compression is required for WNT/β-catenin signaling in endothelial cells

In our study of endothelial cells, we discovered a striking correlation between cell morphology and WNT/β-catenin signaling. Control endothelial cells with active WNT/β-catenin signaling display a higher cellular/nuclear aspect ratio (the ratio of long:-short axis) as well as smaller cell/nuclear volume compared with the WNT/β-catenin signaling-inactive endothelial cells in Piezo2 knockout MB (Figures 5A, 5C, and S6G). This observation raises the prospect that Sox2$^+$ MB cell ensheathment, pericyte coverage, and vascular basement membrane contribute to the compressed endothelial cell shape in control MB. In support of this notion, Sox2$^+$ MB cell-ensheathed or pericyte-covered endothelial cells display higher cellular/nuclear aspect ratio and smaller cell/nuclear volume compared with endothelial cells not in contact with Sox2$^+$ MB cells or pericytes in control MB (Figure 5D). Volumetric compression can stem from passive physical confinement and active cellular contraction. We found that direct compressive stress decreases endothelial cell volume in a magnitude-dependent manner (Figure S6I). Cell-volume compression promotes WNT/β-catenin signaling by stabilizing the LRP-Axin1 signalosome on the cell membrane, leading to stabilization of β-catenin (Li et al., 2020, 2021). Therefore, we asked whether volumetric compression increases WNT/β-catenin signaling in Wnt ligand-expressing human brain microvascular endothelial cells (HBMECs) (Laksitorini et al., 2019). Indeed, both hypertonicity- and direct compressive stress-induced cell-volume reduction increase nuclear β-catenin and LEF1 in HBMECs (Figures 5E, S6H, and S6I), while hypotonic medium increases cell volume and reduces nuclear β-catenin and LEF1 (Figure S6J). Wnt/β-catenin signaling in endothelial cells promotes expression of Pdgfb,

Figure 5. Piezo2 governs WNT/β-catenin signaling states of Sox2$^+$ MB cells and endothelial cells

(A) β-catenin and Lef1 expression in endothelial cells in MB. Three to five P21 mice from each group were studied for quantification. Each data point represents data from one image. Two-tailed t test; mean ± SEM.

(B) β-catenin expression in Sox2$^+$ MB cells. Five P21 mice from each group were studied. Each data point represents data from one image. Two-tailed t test; mean ± SEM.

(C) Cell and nuclear aspect ratio or volume of endothelial cells in MB. Three P21 mice from each group were studied. Each data point represents data from one clear endothelial cell. Two-side t test; mean ± SEM.

(D) Cellular and nuclear aspect ratio or volume of Sox2$^+$ MB cell-ensheathed or pericyte-covered endothelial cells of control MB. Three P21 mice from each group were studied. Each data point represents data from one random region of interest. Two-side t test; mean ± SEM.

(E) Nuclear β-catenin and LEF1 of human brain microvascular endothelial cells treated with vehicle or polyethylene glycol (PEG) or with or without compressive stress. Three independent experiments from each group were performed. Each data point represents data from one random region of interest. For PEG experiment, two-side t test was used; mean ± SEM. For compressive stress experiment, one-way ANOVA with Tukey's multiple comparisons correction was used; mean ± SEM.

(F) Pdgfb expression in MB. Three P21 mice from each group were studied. Each data point represents data from one image. Two-side t test; mean ± SEM.

See also Figure S6.

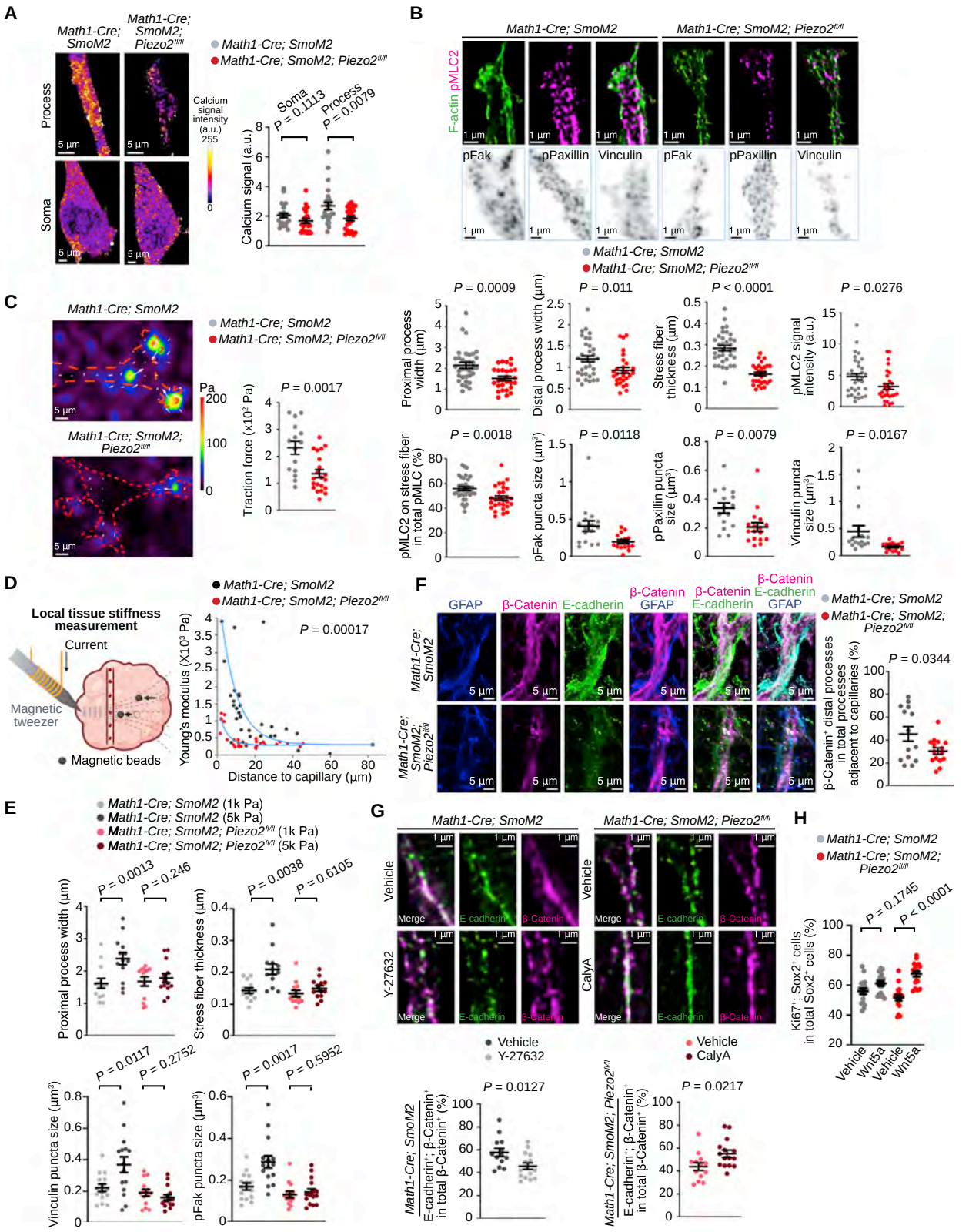

(legend on next page)

which signals from endothelial cells to Pdgfrβ$^+$ pericytes for their recruitment to capillaries (Reis et al., 2012). Consistent with the loss of WNT/β-catenin signaling, endothelial cells in Piezo2 knockout MB display reduced Pdgfb expression (Figure 5F). Therefore, volumetric compression of endothelial cells is associated with Sox2$^+$ MB cell ensheathment and pericyte coverage in BTB. Compressive stress can increase WNT/β-catenin signaling. Loss of WNT/β-catenin signaling in endothelial cells reduces capillary expression of Pdgfb, leading to defective recruitment of pericytes.

Sox2$^+$ MB cells perceive substrate stiffness to promote actomyosin-dependent process growth

As Piezo2 knockout Sox2$^+$ MB cells fail to extend processes to ensheathe capillaries (Figure 2A), we investigated the mechanism by which Piezo2 promotes process growth of Sox2$^+$ MB cells. The growth cone of a neuronal axon generates actomyosin stress fiber-dependent tension and adhesion, both of which are required for axonal elongation (Kerstein et al., 2015). Localized calcium influx at the growth cone regulates axon growth through actomyosin (Gomez and Letourneau, 2014). In breast cancer cells, PIEZO2 promotes stress fiber formation and traction force generation for cell migration and invasion (Pardo-Pastor et al., 2018). PIEZO channel activity increases as a response to substrate stiffening (Murthy et al., 2017). Therefore, we hypothesized that process growth of Sox2$^+$ MB cells depends on Piezo2- and substrate stiffness-dependent tension and adhesion at growth cone-like domains (hereafter referred to as growth cones). Indeed, the growth cones of Sox2$^+$ MB cell processes are Piezo2-dependent "hotspots" that sustain high local intracellular calcium, actomyosin tension, and adhesion (Figures 6A and 6B). Cells perceive and respond to substrate stiffness in part by applying nanonewton-scale traction force onto their substrate. By traction force microscopy, we found that Sox2$^+$ MB cells apply Piezo2-dependent traction force at growth cones but not soma (Figure 6C), revealing growth cones as the primary sites through which Sox2$^+$ MB cells mechanically interact with their microenvironment. The Src family tyrosine kinase Fyn can be activated by increased intracellular calcium. Activated Fyn localizes to focal adhesions to promote stress fiber formation and RhoA activation, which in turn elevates actomyosin tension. Piezo2 promotes the activation of RhoA-GTP and Fyn localization at focal adhesions at Sox2$^+$ MB cell growth cones (Figure S7A), consistent with such roles played by PIEZO2 during breast cancer cell migration (Pardo-Pastor et al., 2018). Control and Piezo2 knockout Sox2$^+$ MB cells display comparable Calpain activity and no SerpinB2 expression (Figure S7A).

While normal brain stiffness is ~200 Pa, human MB develops tissue stiffness of 1.9–75.7 kPa as determined by Raman spectroscopy and atomic force microscopy (Abramczyk and Imiela, 2018). We investigated whether substrate stiffness regulates Sox2$^+$ MB cell process growth. To determine MB tissue stiffness, we custom-built a 3D magnetic tweezer system, which generates a magnetic field to mobilize magnetic beads that have been injected into fresh MB tissue slices. Coupled with live imaging, the extent of magnetic force-induced bead displacement revealed local tissue stiffness (Figure 6D). Strikingly, MB developed tissue stiffness gradient as a function of distance to capillaries. Locoregional tissue stiffness decreased by 2–3 orders of magnitude within a 100 μm range surrounding capillaries (Figure 6D). Piezo2 knockout MB displayed a shallower tissue stiffness gradient (Figure 6D). As MB developed intratumoral tissue stiffness gradient, we asked whether substrate stiffness promotes Sox2$^+$ MB cell process growth in a Piezo2-dependent manner. Indeed, high substrate stiffness promoted stress fiber assembly, focal adhesion formation, and process growth of control but not Piezo2 knockout Sox2$^+$ MB cells (Figure 6E). Decreasing actomyosin tension using ROCK inhibitor Y-27632 decreased the process growth of control Sox2$^+$ MB cells (Figure S7B) while increasing

Figure 6. Piezo2 regulates actomyosin-dependent cellular process growth and is required for β-catenin sequestration to maintain quiescence of Sox2$^+$ MB cells

(A) Piezo2 sustains intracellular calcium level at distal processes but not soma of Sox2$^+$ MB cells cultured on 5k Pa substrate. Cells from 3 P21 mice were studied in each group. Each data point represents one cell. Two-side t test; mean ± SEM.

(B) Piezo2 promotes the assembly of stress fiber and Vinculin, and phosphorylation of myosin light chain II (MLC2), Fak, and Paxillin at growth cones of Sox2$^+$ MB cell processes. Cells from 3 P21 mice were cultured on 5k Pa substrate and studied in each group. Each data point represents measurement from one process. Two-side t test; mean ± SEM.

(C) Traction force microscopy shows that Sox2$^+$ MB cells apply force on their substrate at growth cones, a mechanical property dependent on Piezo2. Arrow length and direction indicate amplitude and direction of Sox2$^+$ MB cell-generated traction force, respectively. Cells from three P21 mice were cultured on 5k Pa substrate and studied in each group. Each data point represents one cell. Two-sided t test; mean ± SEM.

(D) The 3D magnetic tweezer system applies magnetic force to mobilize magnetic beads, the displacement of which determines locoregional tissue stiffness. Three P21 mice from each group were studied. Each data point represents measurement from one magnetic bead. Two sample t test. Exponential model for curve fitting.

(E) Substrate stiffness increases cellular process growth, stress fiber thickness, and focal adhesion size in a Piezo2-dependent manner in Sox2$^+$ MB cells cultured at 1k and 5k Pa stiffness. Cells from three P21 mice were studied in each group. Each data point represents measurement from one process. Two-sided t test; mean ± SEM.

(F) β-catenin and E-cadherin at distal processes of GFAP$^+$ Sox2$^+$ MB cells. Three P21 mice from each group were studied. Each data point represents data from one image. Two-tailed t test; mean ± SEM.

(G) β-catenin and E-cadherin at processes of control Sox2$^+$ MB cells treated with vehicle or Y-27632, or Piezo2 knockout Sox2$^+$ MB cells treated with vehicle or CalyA. Cells from three P21 mice were cultured on 5k Pa substrate and studied in each group. Each data point represents measurement from one process area. Two-sided t test; mean ± SEM.

(H) Quantification of the fraction of Ki67$^+$ cycling Sox2$^+$ MB cells treated with vehicle or Wnt5a. Cells from three P21 mice were cultured on 5k Pa substrate and studied in each group. Each data point represents data from one image. Two-sided t test; mean ± SEM.

See also Figures S7 and S8.

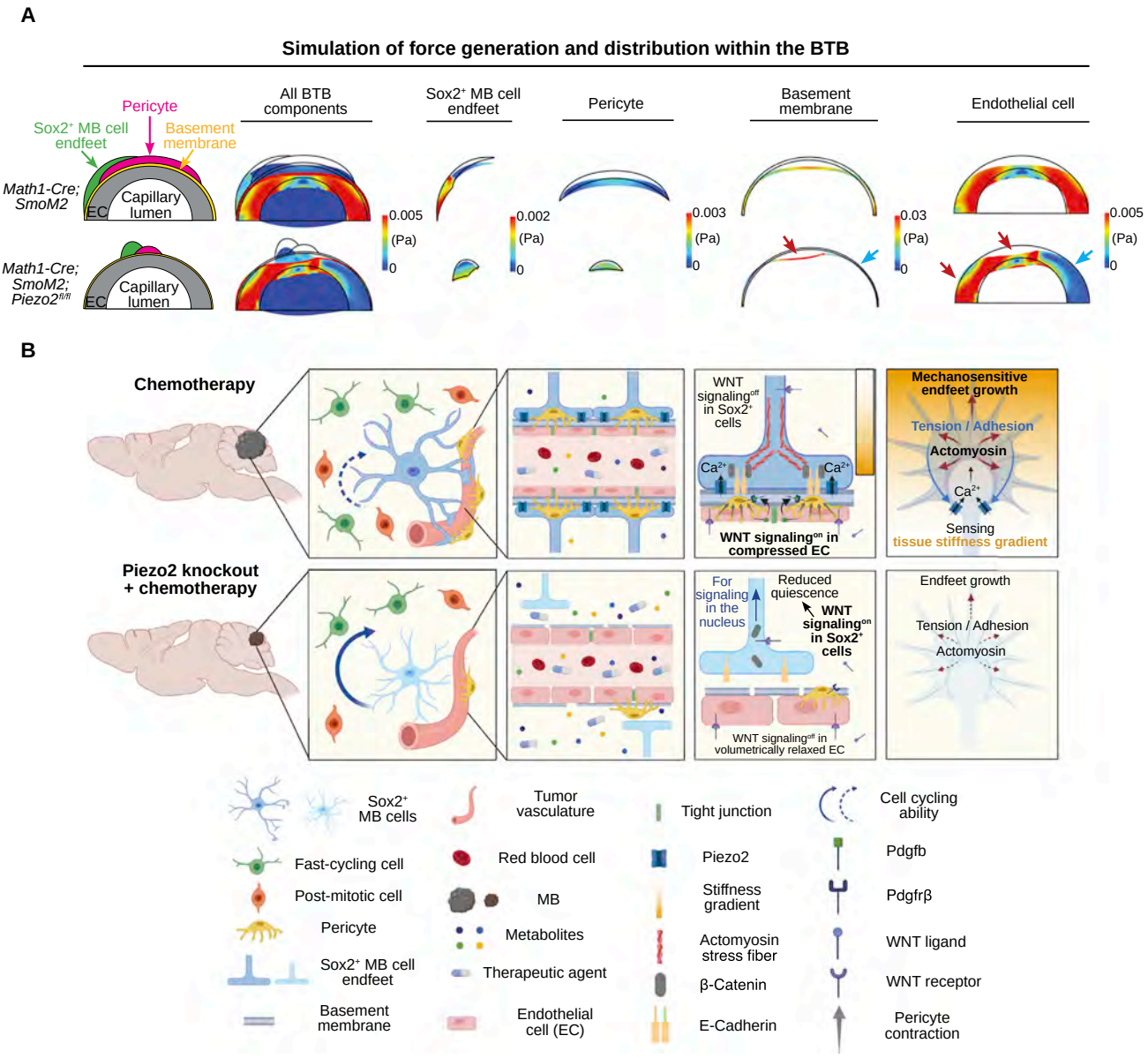

Figure 7. Piezo2 regulates force generation and distribution within the BTB

(A) Simulation of force generation and distribution within the BTB.

(B) A schematic demonstrates that Sox2$^+$ MB cells project endfeet to ensheathe capillaries in BTB. Piezo2 knockout disrupts BTB by reducing Sox2$^+$ MB cell and pericyte coverage on capillaries and compromising basement membrane and tight junction. High substrate stiffness promotes actomyosin assembly, tension, and adhesion at Sox2$^+$ MB cell growth cones, which increase process growth and allow β-catenin and E-cadherin complex formation to prevent WNT/β-catenin signaling in Sox2$^+$ MB cells. Piezo2 knockout mechanically relaxes Sox2$^+$ MB cell growth cones, which suppresses process growth and releases β-catenin to license Sox2$^+$ MB cells for WNT/β-catenin signaling. Volumetric compression, which is associated with Sox2$^+$ MB cell endfeet ensheathment and pericyte coverage, is required for WNT/β-catenin signaling in endothelial cells. Piezo2 knockout disrupts BTB and decreases Sox2$^+$ MB cell quiescence, thereby elevating the chemosensitivity of MB.

See also Figures S8 and S9.

actomyosin tension using Calyculin A (CalyA) rescued the process growth of Piezo2 knockout Sox2$^+$ MB cells (Figure S7C). Together, these data show that Piezo2 perceives substrate stiffness to increase actomyosin-dependent tension and adhesion at growth cones, which promotes process growth of Sox2$^+$ MB cells.

Piezo2 is required for β-catenin sequestration to maintain quiescence of Sox2$^+$ MB cells

Actomyosin tension promotes E-cadherin/β-catenin complex formation to maintain cell-cell adhesion, a process that restricts β-catenin from entering nucleus to activate WNT/β-catenin signaling (Hall et al., 2019). Given that Piezo2 knockout

Sox2$^+$ MB cells are shifted toward a WNT/β-catenin-active state *in vivo* (Figure 5B), we hypothesized that Piezo2-dependent actomyosin tension at cellular processes sequesters β-catenin with E-cadherin to prevent WNT/β-catenin signaling activation. In support of this hypothesis, Piezo2 knockout decreases E-cadherin/β-catenin co-localization at distal processes and increases β-catenin distribution at soma of Sox2$^+$ MB cells (Figures 6F and S7D). Decreasing actomyosin tension using ROCK inhibitor Y-27632 suppresses E-cadherin/β-catenin co-localization at the processes of control Sox2$^+$ MB cells while increasing actomyosin tension using CalyA promotes E-cadherin/β-catenin co-localization at the processes of Piezo2 knockout Sox2$^+$ MB cells (Figure 6G). Treating Sox2$^+$ MB cells with Wnt5a, a Wnt ligand present in MB microenvironment (Figure S6E), activates WNT/β-catenin signaling and increases cell cycling in Piezo2 knockout but not control Sox2$^+$ MB cells (Figures 6H and S7E). Therefore, Piezo2 is required for actomyosin-dependent β-catenin sequestration to prevent WNT/β-catenin signaling activation in Sox2$^+$ MB cells, a state that maintains their quiescence.

Piezo2 regulates force generation and distribution within the BTB

Pericytes, which protrude processes to cover capillaries, display prominent expression of phosphorylated myosin light chain 2 (MLC2), a marker of cell contractility (Figure S8A), highlighting pericytes as the main source of mechanical stress within the BTB. Since Sox2$^+$ MB cells ensheathe endothelial cells, pericytes generate mechanical stress, and endothelial cells are volumetrically compressed, we postulated that BTB is a mechanically integrated structure. To holistically investigate mechanical stress within BTB, we computationally constructed a multilayered structure consisting of Sox2$^+$ MB cell endfeet, pericyte, vascular basement membrane, and endothelial cells. We applied pericyte-generated contractile force in this structure (see STAR Methods). The simulation of mechanical stress within BTB of control and Piezo2 knockout MB offered several insights (Figure 7A; Video S1). First, pericyte-generated stress is transmitted to all cellular and extracellular BTB components, including Sox2$^+$ MB cell endfeet, pericyte, basement membrane, and endothelial cells (Figure 7A). Second, Sox2$^+$ MB cell ensheathment helps localize pericyte-generated stress within the ensheathed area (Figure 7A). Third, the basement membrane converts pericyte contraction into compressive stress applied to endothelial cells (Figure 7A). Fourth, basement membrane bears most mechanical stress, including compression and tension, within the BTB (Figures 7A, S8B, and S9). In Piezo2 knockout BTB, the ensheathed basement membrane and endothelial cells bear high localized stress (Figure 7A, red arrow), while nonensheathed basement membrane and endothelial cells experience low stress (Figure 7A, blue arrow). The simulation data support that BTB is a mechanically integrated structure that generates and distributes stress, and such mechanical homeostasis is governed by Piezo2.

DISCUSSION

Overcoming the BTB for therapeutics to achieve pharmacologically meaningful concentrations in the brain is an unmet clinical need. Tumor cell differentiation into endothelial cells (Hu et al., 2016; Ricci-Vitiani et al., 2010; Wang et al., 2010) or pericytes (Cheng et al., 2013; Zhou et al., 2017) has been shown to contribute to the BTB, thereby promoting the chemoresistance of glioblastoma. However, it is unknown whether glioblastoma cells directly contribute to BTB without transdifferentiation into endothelial cells or pericytes. Here we report Sox2$^+$ MB cells as direct contributors to BTB formation and function, Piezo2 as an orchestrator of mechano-chemical signaling that governs Sox2$^+$ MB cell and BTB states, and the BTB as a mechanically integrated unit (Figure 7B). Sox2$^+$ MB cells comprise a small population of the total tumor cells in SHH MB (Vanner et al., 2014). While Piezo2 knockout altered the mechanical and quiescent properties of Sox2$^+$ MB cells and comprised the BTB, the overall numbers of mitotic tumor cells are comparable between control and Piezo2 knockout MB (Figures S5A and S5B), demonstrating that Piezo2 knockout does not alter the proliferative output of MB at therapy-naive state. This is consistent with the comparable survival between control and Piezo2 knockout MB-bearing mice (Figure S5C). Therefore, the primary consequence of Piezo2 knockout appears to be elevating MB chemosensitivity. While we uncovered the role of Piezo2 in Sox2$^+$ MB cells, the overall significance of this neoplastic cell population in BTB may be elucidated by genetically depleting such cells in MB. MB comprises four subgroups (SHH, WNT, group 3, group 4), each characterized by distinct genomic, epigenetic, transcriptomic, and clinical features (Hovestadt et al., 2019; Riemondy et al., 2022). As our study focused on SHH MB, it would be of clinical significance to investigate whether group 3 or 4-MB cells, which express *PIEZO1* (Figure S5F), utilize mechanotransduction to govern their BTB. Recent studies investigated Piezo channels in Wnt/β-catenin signaling. During bone development, Piezo1/2 perceive mechanical signals to increase β-catenin activity by promoting NFAT/YAP1/β-catenin complex formation (Zhou et al., 2020). Hydrostatic pressure regulates the expression of Wnt ligands (WNT5b and WNT16) through PIEZO1 in stem cells from human teeth (Miyazaki et al., 2019). Herein, Piezo2 promotes actomyosin tension to sequester β-catenin thereby preventing ectopic Wnt/β-catenin signaling (rather than activating this pathway) in the context of brain cancer.

We suggest that Sox2$^+$ MB cell ensheathment, pericyte force, and high locoregional tissue stiffness maintain a mechanical niche for the BTB. Perturbing a component of the mechanical niche, such as endfeet ensheathment, pericyte coverage or contractility, or basement membrane integrity, can compromise the brain barrier. As Sox2$^+$ MB cells display mechanosensitivity to solid and shear stress (Figures 1G and 1H), mechanosensitive ion channels may allow tumor cells to respond to multimodal mechanical cues in the microenvironment. Indeed, PIEZO2 regulates stress fiber formation and traction force generation in breast cancer cells in favor of brain metastasis (Pardo-Pastor et al., 2018). Additionally, the mechanosensitive ion channel TRPM7 governs shear stress-dependent tumor cell intravasation and the establishment of metastatic lesions (Yankaskas et al., 2021).

We reported that glioma cells express PIEZO1 to perceive tissue mechanics and promote tumor stiffening and proliferation (Chen et al., 2018). Given that glioma cells display complex

cellular processes, they may also physically cover blood vessels to form a mechanosensitive BTB. CNS metastasis occurs in ~20% of all cancer patients, with the highest occurrences in lung cancer, breast cancer, and melanoma (Achrol et al., 2019). While small-cell lung cancer is sensitive to chemotherapy that combines etoposide and cisplatin, neither drug penetrates the brain barrier, leaving brain metastases unaffected by chemotherapy (Sarkaria et al., 2018). It is imperative to investigate whether metastatic cells in the brain develop mechanosensitive BTB to prevent access to systemically administered drugs. Vasculature has been intensely studied as an anatomical and signaling niche. Our discovery of tissue stiffness gradient adjacent to blood vessels opens investigations to determine whether vasculature-related cell behaviors (tumor invasion along vascular pathways, stemness, metabolic zonation, just to name a few) are regulated by this newfound mechanical trait. Furthermore, the immune microenvironment may be altered by a more permeable BTB. Future investigations are warranted to profile the infiltration and functional states of immune cell types and determine the benefit of using immunotherapy to treat mice bearing Piezo2 knockout MB. Another implication of our work is that mechanics may regulate the BBB of brain disorders. Multiple clinical trials use transcranial focused ultrasound (t-FUS)-activation of microbubbles to transiently open the BBB or BTB to treat brain disorders or tumors (Sprowls et al., 2019). It is important to determine whether mechanotransduction interference underlies the utility of these clinical procedures.

In conclusion, our study reveals that mechanosensitive tumor cells construct the BTB in SHH MB and defines a Piezo2-mediated mechanism that controls the accessibility of systemically administered therapeutics to brain tumors.

STAR★METHODS

Detailed methods are provided in the online version of this paper and include the following:

- KEY RESOURCES TABLE
- RESOURCE AVAILABILITY
  - Lead contact
  - Materials availability
  - Data and code availability
- EXPERIMENTAL MODEL AND SUBJECT DETAILS
  - Mouse
  - Cell cultures
- METHOD DETAILS
  - Immunohistochemistry and image quantifications
  - Transmission electron microscopy (TEM)
  - Hypertonicity and hypotonicity treatment to endothelial cells
  - Generating coverslips with various levels of substrate stiffness
  - Applying axial compression using a compressive load system
  - Mouse $Sox2^{+}$ MB cell isolation, culture, and immunocytochemistry
  - Traction force microscopy
  - Ratiometric calcium imaging
  - RNA extraction, reverse transcription, and real-time RT-PCR
  - Electrophysiology
  - Tissue stiffness measurement by 3D magnetic tweezer system
  - Cell stretching and calcium imaging
  - Calpain activity
  - Western blotting
  - MALDI TOF MS imaging and LC-MS/MS
  - Fluorescence in situ hybridization (FISH)
  - Single-cell RNA sequencing (scRNA-seq) and analysis
  - Patient cohort and survival analysis
  - Lentivirus production
  - Xenograft study
  - BTB permeability assay
  - Computational simulation of mechanical stress within the BTB
- QUANTIFICATION AND STATISTICAL ANALYSIS

SUPPLEMENTAL INFORMATION

Supplemental information can be found online at https://doi.org/10.1016/j.neuron.2022.10.007.

ACKNOWLEDGMENTS

This work is supported by SickKids Foundation, Arthur and Sonia Labatt Brain Tumour Research Centre, Garron Family Cancer Centre, Sontag Foundation, Cancer Research Society, Canadian Cancer Society, b.r.a.i.n.child, Meagan's HUG, Natural Sciences and Engineering Research Council Discovery Grant, Ontario Institute for Cancer Research Translational Research Initiative, Early Researcher Award, and Canadian Institute of Health Research Project Grants to X.H., a Garron Family Cancer Centre Pitblado Discovery Grant to L.-Y.W. and X.H., Canadian Institute of Health Research project grants (PJT-156034 and PJT-156439) and a Natural Sciences and Engineering Research Council grant (RGPIN-2017-06665) to L.-Y.W., and a National Natural Science Foundation of China grant (81770781) to X.L. X.C. is supported by a SickKids Restracomp Scholarship. A.M. is supported by an Ontario Graduate Scholarship. X.W.is supported by a Brain Tumour Foundation of Canada Dunn with Cancer Research Fellowship, a SickKids Lap-Chee Tsui Fellowship, and an Inspiration Award from the Hopper-Belmont Foundation. Y.X.C. and K.V. are supported by the Sloan Foundation CSURP program. Y.H. and R.A. are supported by the PSC-CUNY Research Award Program. We thank Paul Paroutis and Kimberly Lau at SickKids Imaging Facility. We thank Tong Wang, Sheng Zhang, Jorge Morales, Zhi-Lun Liu, Avani Butala, and Elvina Abzalimov at CUNY for technical support. We thank Ali Darbandi at SickKids Nanoscale Biomedical Imaging Facility for TEM imaging and Savo Bajic for BTB force simulation. We thank Drs. Joan Massagué and Adrienne Boire for providing MDA-MB-231 cells. We thank Wei Wang for technical assistance and Huang lab members for comments on the manuscript. Schematics are created using BioRender. X.H. thanks the love and support from Lucas Huang and Liam Huang. L.-Y.W. is Canada Research Chair in Brain Development and Disorders. X.H. is a Catalyst Scholar at The Hospital for Sick Children and Canada Research Chair in Cancer Biophysics.

AUTHOR CONTRIBUTIONS

X.H. directed the study. Experimental design, data acquisition, and interpretation, X.C., A.M., S.W., X.W., H.-K.M., Wenkun Dou, Z.G., J.C., Weifan Dong, J.J.F., Y.X., K.T., H.Z., Y.X.C., K.V., A.F., S.A.K., H.L., Q.Y., J.E.S., Z.D., M.H., P.P., K.J., L.K.D., J.Z., V.R., H.J.S., P.B.D., M.D.T., L.-Y.W., C.-c.H., R.A., Y.H., Y.S., X.L., and X.H.; manuscript writing, X.C., A.M., S.W., and X.H.

DECLARATION OF INTERESTS

The authors declare no competing interests.

INCLUSION AND DIVERSITY

We support inclusive, diverse, and equitable conduct of research.

Received: March 25, 2022
Revised: August 30, 2022
Accepted: October 4, 2022
Published: November 1, 2022

REFERENCES

Abramczyk, H., and Imiela, A. (2018). The biochemical, nanomechanical and chemometric signatures of brain cancer. Spectrochim. Acta A Mol. Biomol. Spectrosc. *188*, 8–19.

Achrol, A.S., Rennert, R.C., Anders, C., Soffietti, R., Ahluwalia, M.S., Nayak, L., Peters, S., Arvold, N.D., Harsh, G.R., Steeg, P.S., et al. (2019). Brain metastases. Nat. Rev. Dis. Primers *5*, 5.

Aibar, S., González-Blas, C.B., Moerman, T., Huynh-Thu, V.A., Imrichova, H., Hulselmans, G., Rambow, F., Marine, J.C., Geurts, P., Aerts, J., et al. (2017). SCENIC: single-cell regulatory network inference and clustering. Nat. Methods *14*, 1083–1086.

Armulik, A., Genové, G., Mäe, M., Nisancioglu, M.H., Wallgard, E., Niaudet, C., He, L., Norlin, J., Lindblom, P., Strittmatter, K., et al. (2010). Pericytes regulate the blood-brain barrier. Nature *468*, 557–561.

Arnold, K., Sarkar, A., Yram, M.A., Polo, J.M., Bronson, R., SenGupta, S., Seandel, M., Geijsen, N., and Hochedlinger, K. (2011). Sox2(+) adult stem and progenitor cells are important for tissue regeneration and survival of mice. Cell Stem Cell *9*, 317–329.

Arvanitis, C.D., Ferraro, G.B., and Jain, R.K. (2020). The blood-brain barrier and blood-tumour barrier in brain tumours and metastases. Nat. Rev. Cancer *20*, 26–41.

Baeten, K.M., and Akassoglou, K. (2011). Extracellular matrix and matrix receptors in blood-brain barrier formation and stroke. Dev. Neurobiol. *71*, 1018–1039.

Ben-Zvi, A., Lacoste, B., Kur, E., Andreone, B.J., Mayshar, Y., Yan, H., and Gu, C. (2014). Mfsd2a is critical for the formation and function of the blood-brain barrier. Nature *509*, 507–511.

Boire, A., Zou, Y., Shieh, J., Macalinao, D.G., Pentsova, E., and Massagué, J. (2017). Complement component 3 adapts the cerebrospinal fluid for leptomeningeal metastasis. Cell *168*, 1101–1113.e13.

Boyle, F.M., Eller, S.L., and Grossman, S.A. (2004). Penetration of intra-arterially administered vincristine in experimental brain tumor. Neuro. Oncol *6*, 300–305.

Byfield, F.J., Reen, R.K., Shentu, T.P., Levitan, I., and Gooch, K.J. (2009). Endothelial actin and cell stiffness is modulated by substrate stiffness in 2D and 3D. J. Biomech. *42*, 1114–1119.

Cahalan, S.M., Lukacs, V., Ranade, S.S., Chien, S., Bandell, M., and Patapoutian, A. (2015). Piezo1 links mechanical forces to red blood cell volume. eLife *4*, e07370.

Cavalli, F.M.G., Remke, M., Rampasek, L., Peacock, J., Shih, D.J.H., Luu, B., Garzia, L., Torchia, J., Nor, C., Morrissy, A.S., et al. (2017). Intertumoral heterogeneity within medulloblastoma subgroups. Cancer Cell *31*, 737–754.e6.

Chen, J., and Kumar, S. (2017). Biophysical regulation of cancer stem/initiating cells: implications for disease mechanisms and translation. Curr. Opin. Biomed Eng. *1*, 87–95.

Chen, X., Wanggou, S., Bodalia, A., Zhu, M., Dong, W., Fan, J.J., Yin, W.C., Min, H.K., Hu, M., Draghici, D., et al. (2018). A feedforward mechanism mediated by mechanosensitive ion channel PIEZO1 and tissue mechanics promotes glioma aggression. Neuron *100*, 799–815.e7.

Cheng, L., Huang, Z., Zhou, W., Wu, Q., Donnola, S., Liu, J.K., Fang, X., Sloan, A.E., Mao, Y., Lathia, J.D., et al. (2013). Glioblastoma stem cells generate vascular pericytes to support vessel function and tumor growth. Cell *153*, 139–152.

Chi, S., Cui, Y., Wang, H., Jiang, J., Zhang, T., Sun, S., Zhou, Z., Zhong, Y., and Xiao, B. (2022). Astrocytic Piezo1-mediated mechanotransduction determines adult neurogenesis and cognitive functions. Neuron *110*, 2984–2999.e8.

Daneman, R., Zhou, L., Kebede, A.A., and Barres, B.A. (2010). Pericytes are required for blood-brain barrier integrity during embryogenesis. Nature *468*, 562–566.

Dessalles, C.A., Babataheri, A., and Barakat, A.I. (2021). Pericyte mechanics and mechanobiology. J. Cell Sci. *134*, jcs240226.

Domingo-Almenara, X., Montenegro-Burke, J.R., Ivanisevic, J., Thomas, A., Sidibé, J., Teav, T., Guijas, C., Aisporna, A.E., Rinehart, D., Hoang, L., et al. (2018). XCMS-MRM and METLIN-MRM: a cloud library and public resource for targeted analysis of small molecules. Nat. Methods *15*, 681–684.

Donovan, L.K., Delaidelli, A., Joseph, S.K., Bielamowicz, K., Fousek, K., Holgado, B.L., Manno, A., Srikanthan, D., Gad, A.Z., Van Ommeren, R., et al. (2020). Locoregional delivery of CAR T cells to the cerebrospinal fluid for treatment of metastatic medulloblastoma and ependymoma. Nat. Med. *26*, 720–731.

Doumpas, N., Lampart, F., Robinson, M.D., Lentini, A., Nestor, C.E., Cantù, C., and Basler, K. (2019). TCF/LEF dependent and independent transcriptional regulation of Wnt/beta-catenin target genes. EMBO J. *38*, e98873.

Durinck, S., Spellman, P.T., Birney, E., and Huber, W. (2009). Mapping identifiers for the integration of genomic datasets with the R/Bioconductor package biomaRt. Nat. Protoc. *4*, 1184–1191.

Fagotto, F., Glück, U., and Gumbiner, B.M. (1998). Nuclear localization signal-independent and importin/karyopherin-independent nuclear import of beta-catenin. Curr. Biol. *8*, 181–190.

Francisco, M.A., Wanggou, S., Fan, J.J., Dong, W., Chen, X., Momin, A., Abeysundara, N., Min, H.K., Chan, J., McAdam, R., et al. (2020). Chloride intracellular channel 1 cooperates with potassium channel EAG2 to promote medulloblastoma growth. J. Exp. Med. *217*, e20190971.

Garzia, L., Kijima, N., Morrissy, A.S., De Antonellis, P., Guerreiro-Stucklin, A., Holgado, B.L., Wu, X., Wang, X., Parsons, M., Zayne, K., et al. (2018). A hematogenous route for medulloblastoma leptomeningeal metastases. Cell *172*, 1050–1062.e14.

Gomez, T.M., and Letourneau, P.C. (2014). Actin dynamics in growth cone motility and navigation. J. Neurochem. *129*, 221–234.

Goodrich, L.V., Milenković, L., Higgins, K.M., and Scott, M.P. (1997). Altered neural cell fates and medulloblastoma in mouse patched mutants. Science *277*, 1109–1113.

Griveau, A., Seano, G., Shelton, S.J., Kupp, R., Jahangiri, A., Obernier, K., Krishnan, S., Lindberg, O.R., Yuen, T.J., Tien, A.C., et al. (2018). A glial signature and Wnt7 signaling regulate glioma-vascular interactions and tumor microenvironment. Cancer Cell *33*, 874–889.e7.

Gudipaty, S.A., Lindblom, J., Loftus, P.D., Redd, M.J., Edes, K., Davey, C.F., Krishnegowda, V., and Rosenblatt, J. (2017). Mechanical stretch triggers rapid epithelial cell division through Piezo1. Nature *543*, 118–121.

Hall, C.N., Reynell, C., Gesslein, B., Hamilton, N.B., Mishra, A., Sutherland, B.A., O'Farrell, F.M., Buchan, A.M., Lauritzen, M., and Attwell, D. (2014). Capillary pericytes regulate cerebral blood flow in health and disease. Nature *508*, 55–60.

Hall, E.T., Hoesing, E., Sinkovics, E., and Verheyen, E.M. (2019). Actomyosin contractility modulates Wnt signaling through adherens junction stability. Mol. Biol. Cell *30*, 411–426.

Hao, Y., Hao, S., Andersen-Nissen, E., Mauck, W.M., 3rd, Zheng, S., Butler, A., Lee, M.J., Wilk, A.J., Darby, C., Zager, M., et al. (2021). Integrated analysis of multimodal single-cell data. Cell *184*, 3573–3587.e29.

Hovestadt, V., Smith, K.S., Bihannic, L., Filbin, M.G., Shaw, M.L., Baumgartner, A., DeWitt, J.C., Groves, A., Mayr, L., Weisman, H.R., et al.

(2019). Resolving medulloblastoma cellular architecture by single-cell genomics. Nature *572*, 74–79.

Hu, B., Wang, Q., Wang, Y.A., Hua, S., Sauvé, C.G., Ong, D., Lan, Z.D., Chang, Q., Ho, Y.W., Monasterio, M.M., et al. (2016). Epigenetic activation of WNT5A drives glioblastoma stem cell differentiation and invasive growth. Cell *167*, 1281–1295.e18.

Huang, X., Ketova, T., Litingtung, Y., and Chiang, C. (2010). Isolation, enrichment, and maintenance of medulloblastoma stem cells. J. Vis. Exp. *43*, 2086.

Huber, W., Carey, V.J., Gentleman, R., Anders, S., Carlson, M., Carvalho, B.S., Bravo, H.C., Davis, S., Gatto, L., Girke, T., et al. (2015). Orchestrating high-throughput genomic analysis with Bioconductor. Nat. Methods *12*, 115–121.

Hui, C.C., and Joyner, A.L. (1993). A mouse model of Greig cephalopolysyndactyly syndrome: the extra-toesJ mutation contains an intragenic deletion of the Gli3 gene. Nat. Genet. *3*, 241–246.

Jandura, A., Hu, J., Wilk, R., and Krause, H.M. (2017). High resolution fluorescent in situ hybridization in drosophila embryos and tissues using tyramide signal amplification. J. Vis. Exp. *128*, 56281.

Ji, Z., and Ji, H. (2016). TSCAN: pseudo-time reconstruction and evaluation in single-cell RNA-seq analysis. Nucleic Acids Res. *44*, e117.

Jiang, Y., Yang, X., Jiang, J., and Xiao, B. (2021). Structural designs and Mechanogating mechanisms of the mechanosensitive piezo channels. Trends Biochem. Sci. *46*, 472–488.

Juraschka, K., and Taylor, M.D. (2019). Medulloblastoma in the age of molecular subgroups: a review. J. Neurosurg. Pediatr. *24*, 353–363.

Kerstein, P.C., Nichol, R.H., and Gomez, T.M. (2015). Mechanochemical regulation of growth cone motility. Front. Cell. Neurosci. *9*, 244.

Kumar, A., Mazzanti, M., Mistrik, M., Kosar, M., Beznoussenko, G.V., Mironov, A.A., Garrè, M., Parazzoli, D., Shivashankar, G.V., Scita, G., et al. (2014). ATR mediates a checkpoint at the nuclear envelope in response to mechanical stress. Cell *158*, 633–646.

La Manno, G., Soldatov, R., Zeisel, A., Braun, E., Hochgerner, H., Petukhov, V., Lidschreiber, K., Kastriti, M.E., Lönnerberg, P., Furlan, A., et al. (2018). RNA velocity of single cells. Nature *560*, 494–498.

Laksitorini, M.D., Yathindranath, V., Xiong, W., Hombach-Klonisch, S., and Miller, D.W. (2019). Modulation of Wnt/beta-catenin signaling promotes blood-brain barrier phenotype in cultured brain endothelial cells. Sci. Rep. *9*, 19718.

Langen, U.H., Ayloo, S., and Gu, C. (2019). Development and cell biology of the blood-brain barrier. Annu. Rev. Cell Dev. Biol. *35*, 591–613.

Li, X., Han, L., Nookaew, I., Mannen, E., Silva, M.J., Almeida, M., and Xiong, J. (2019). Stimulation of Piezo1 by mechanical signals promotes bone anabolism. eLife *8*, e49631.

Li, Y., Chen, M., Hu, J., Sheng, R., Lin, Q., He, X., and Guo, M. (2021). Volumetric compression induces intracellular crowding to control intestinal organoid growth via Wnt/beta-catenin signaling. Cell Stem Cell *28*, 63–78.e67.

Li, Y., Mao, A.S., Seo, B.R., Zhao, X., Gupta, S.K., Chen, M., Han, Y.L., Shih, T.Y., Mooney, D.J., and Guo, M. (2020). Compression-induced dedifferentiation of adipocytes promotes tumor progression. Sci. Adv. *6*, eaax5611.

Ligon, K.L., Huillard, E., Mehta, S., Kesari, S., Liu, H., Alberta, J.A., Bachoo, R.M., Kane, M., Louis, D.N., Depinho, R.A., et al. (2007). Olig2-regulated lineage-restricted pathway controls replication competence in neural stem cells and malignant glioma. Neuron *53*, 503–517.

Liu, H., MacQueen, L.A., Usprech, J.F., Maleki, H., Sider, K.L., Doyle, M.G., Sun, Y., and Simmons, C.A. (2018). Microdevice arrays with strain sensors for 3D mechanical stimulation and monitoring of engineered tissues. Biomaterials *172*, 30–40.

Love, M.I., Huber, W., and Anders, S. (2014). Moderated estimation of fold change and dispersion for RNA-seq data with DESeq2. Genome Biol. *15*, 550.

Menezes, M.J., McClenahan, F.K., Leiton, C.V., Aranmolate, A., Shan, X., and Colognato, H. (2014). The extracellular matrix protein laminin alpha2 regulates the maturation and function of the blood-brain barrier. J. Neurosci. *34*, 15260–15280.

Miyazaki, A., Sugimoto, A., Yoshizaki, K., Kawarabayashi, K., Iwata, K., Kurogoushi, R., Kitamura, T., Otsuka, K., Hasegawa, T., Akazawa, Y., et al. (2019). Coordination of WNT signaling and ciliogenesis during odontogenesis by piezo type mechanosensitive ion channel component 1. Sci. Rep. *9*, 14762.

Mizuno, H., Nakanishi, Y., Ishii, N., Sarai, A., and Kitada, K. (2009). A signature-based method for indexing cell cycle phase distribution from microarray profiles. BMC Genomics *10*, 137.

Momin, A., Bahrampour, S., Min, H.K., Chen, X., Wang, X., Sun, Y., and Huang, X. (2021). Channeling force in the brain: mechanosensitive ion channels choreograph mechanics and malignancies. Trends Pharmacol. Sci. *42*, 367–384.

Murthy, S.E., Dubin, A.E., and Patapoutian, A. (2017). Piezos thrive under pressure: mechanically activated ion channels in health and disease. Nat. Rev. Mol. Cell Biol. *18*, 771–783.

Northcott, P.A., Buchhalter, I., Morrissy, A.S., Hovestadt, V., Weischenfeldt, J., Ehrenberger, T., Gröbner, S., Segura-Wang, M., Zichner, T., Rudneva, V.A., et al. (2017). The whole-genome landscape of medulloblastoma subtypes. Nature *547*, 311–317.

Northey, J.J., Przybyla, L., and Weaver, V.M. (2017). Tissue force programs cell fate and tumor aggression. Cancer Discov. *7*, 1224–1237.

O'Brown, N.M., Megason, S.G., and Gu, C. (2019). Suppression of transcytosis regulates zebrafish blood-brain barrier function. eLife *8*, e47326.

Pardo-Pastor, C., Rubio-Moscardo, F., Vogel-Gonzalez, M., Serra, S.A., Afthinos, A., Mrkonjic, S., Destaing, O., Abenza, J.F., Fernandez-Fernandez, J.M., Trepat, X., et al. (2018). Piezo2 channel regulates RhoA and actin cytoskeleton to promote cell mechanobiological responses. Proc. Natl. Acad. Sci. USA *115*, 1925–1930.

Phoenix, T.N., Patmore, D.M., Boop, S., Boulos, N., Jacus, M.O., Patel, Y.T., Roussel, M.F., Finkelstein, D., Goumnerova, L., Perreault, S., et al. (2016). Medulloblastoma genotype dictates blood brain barrier phenotype. Cancer Cell *29*, 508–522.

Prieve, M.G., and Waterman, M.L. (1999). Nuclear localization and formation of beta-catenin-lymphoid enhancer factor 1 complexes are not sufficient for activation of gene expression. Mol. Cell. Biol. *19*, 4503–4515.

Ramaswamy, V., and Taylor, M.D. (2019). Bioinformatic strategies for the genomic and epigenomic characterization of brain tumors. Methods Mol. Biol. *1869*, 37–56.

Ranade, S.S., Qiu, Z., Woo, S.H., Hur, S.S., Murthy, S.E., Cahalan, S.M., Xu, J., Mathur, J., Bandell, M., Coste, B., et al. (2014a). Piezo1, a mechanically activated ion channel, is required for vascular development in mice. Proc. Natl. Acad. Sci. USA *111*, 10347–10352.

Ranade, S.S., Woo, S.H., Dubin, A.E., Moshourab, R.A., Wetzel, C., Petrus, M., Mathur, J., Bégay, V., Coste, B., Mainquist, J., et al. (2014b). Piezo2 is the major transducer of mechanical forces for touch sensation in mice. Nature *516*, 121–125.

Reis, M., Czupalla, C.J., Ziegler, N., Devraj, K., Zinke, J., Seidel, S., Heck, R., Thom, S., Macas, J., Bockamp, E., et al. (2012). Endothelial Wnt/beta-catenin signaling inhibits glioma angiogenesis and normalizes tumor blood vessels by inducing PDGF-B expression. J. Exp. Med. *209*, 1611–1627.

Reuten, R., Zendehroud, S., Nicolau, M., Fleischhauer, L., Laitala, A., Kiderlen, S., Nikodemus, D., Wullkopf, L., Nielsen, S.R., McNeilly, S., et al. (2021). Basement membrane stiffness determines metastases formation. Nat. Mater. *20*, 892–903.

Ricci-Vitiani, L., Pallini, R., Biffoni, M., Todaro, M., Invernici, G., Cenci, T., Maira, G., Parati, E.A., Stassi, G., Larocca, L.M., et al. (2010). Tumour vascularization via endothelial differentiation of glioblastoma stem-like cells. Nature *468*, 824–828.

Riemondy, K.A., Venkataraman, S., Willard, N., Nellan, A., Sanford, B., Griesinger, A.M., Amani, V., Mitra, S., Hankinson, T.C., Handler, M.H., et al. (2022). Neoplastic and immune single-cell transcriptomics define subgroup-specific intra-tumoral heterogeneity of childhood medulloblastoma. Neuro. Oncol *24*, 273–286.

Saelens, W., Cannoodt, R., Todorov, H., and Saeys, Y. (2019). A comparison of single-cell trajectory inference methods. Nat. Biotechnol. *37*, 547–554.

Sarkaria, J.N., Hu, L.S., Parney, I.F., Pafundi, D.H., Brinkmann, D.H., Laack, N.N., Giannini, C., Burns, T.C., Kizilbash, S.H., Laramy, J.K., et al. (2018). Is the blood-brain barrier really disrupted in all glioblastomas? A critical assessment of existing clinical data. Neuro. Oncol *20*, 184–191.

Schüller, U., Heine, V.M., Mao, J., Kho, A.T., Dillon, A.K., Han, Y.G., Huillard, E., Sun, T., Ligon, A.H., Qian, Y., et al. (2008). Acquisition of granule neuron precursor identity is a critical determinant of progenitor cell competence to form Shh-induced medulloblastoma. Cancer Cell *14*, 123–134.

Ser, Z., Liu, X., Tang, N.N., and Locasale, J.W. (2015). Extraction parameters for metabolomics from cultured cells. Anal. Biochem. *475*, 22–28.

Smith, C.A., Want, E.J., O'Maille, G., Abagyan, R., and Siuzdak, G. (2006). XCMS: processing mass spectrometry data for metabolite profiling using nonlinear peak alignment, matching, and identification. Anal. Chem. *78*, 779–787.

Sprowls, S.A., Arsiwala, T.A., Bumgarner, J.R., Shah, N., Lateef, S.S., Kielkowski, B.N., and Lockman, P.R. (2019). Improving CNS delivery to brain metastases by blood-tumor barrier disruption. Trends Cancer *5*, 495–505.

Stenzel, D., Franco, C.A., Estrach, S., Mettouchi, A., Sauvaget, D., Rosewell, I., Schertel, A., Armer, H., Domogatskaya, A., Rodin, S., et al. (2011). Endothelial basement membrane limits tip cell formation by inducing Dll4/Notch signalling in vivo. EMBO Rep. *12*, 1135–1143.

Stuart, T., Butler, A., Hoffman, P., Hafemeister, C., Papalexi, E., Mauck, W.M., 3rd, Hao, Y., Stoeckius, M., Smibert, P., and Satija, R. (2019). Comprehensive integration of single-cell data. Cell *177*, 1888–1902.e21.

Sun, W., Chi, S., Li, Y., Ling, S., Tan, Y., Xu, Y., Jiang, F., Li, J., Liu, C., Zhong, G., et al. (2019). The mechanosensitive Piezo1 channel is required for bone formation. eLife *8*, e47454.

Suzuki, H., Kumar, S.A., Shuai, S., Diaz-Navarro, A., Gutierrez-Fernandez, A., De Antonellis, P., Cavalli, F.M.G., Juraschka, K., Farooq, H., Shibahara, I., et al. (2019). Recurrent noncoding U1 snRNA mutations drive cryptic splicing in SHH medulloblastoma. Nature *574*, 707–711.

Sweeney, M.D., Zhao, Z., Montagne, A., Nelson, A.R., and Zlokovic, B.V. (2019). Blood-brain barrier: From physiology to disease and back. Physiol. Rev. *99*, 21–78.

Van den Berge, K., Perraudeau, F., Soneson, C., Love, M.I., Risso, D., Vert, J.P., Robinson, M.D., Dudoit, S., and Clement, L. (2018). Observation weights unlock bulk RNA-seq tools for zero inflation and single-cell applications. Genome Biol. *19*, 24.

Vanner, R.J., Remke, M., Gallo, M., Selvadurai, H.J., Coutinho, F., Lee, L., Kushida, M., Head, R., Morrissy, S., Zhu, X., et al. (2014). Quiescent sox2(+) cells drive hierarchical growth and relapse in sonic hedgehog subgroup medulloblastoma. Cancer Cell *26*, 33–47.

Veerasammy, K., Chen, Y.X., Sauma, S., Pruvost, M., Dansu, D.K., Choetso, T., Zhong, T., Marechal, D., Casaccia, P., Abzalimov, R., et al. (2020). Sample preparation for metabolic profiling using MALDI mass spectrometry imaging. J. Vis. Exp. https://doi.org/10.3791/62008.

Wang, J., Qiu, S., Chen, S., Xiong, C., Liu, H., Wang, J., Zhang, N., Hou, J., He, Q., and Nie, Z. (2015). MALDI-TOF MS imaging of metabolites with a N-(1-naphthyl) ethylenediamine dihydrochloride matrix and its application to colorectal cancer liver metastasis. Anal. Chem. *87*, 422–430.

Wang, R., Chadalavada, K., Wilshire, J., Kowalik, U., Hovinga, K.E., Geber, A., Fligelman, B., Leversha, M., Brennan, C., and Tabar, V. (2010). Glioblastoma stem-like cells give rise to tumour endothelium. Nature *468*, 829–833.

Wang, X., Liu, H., Zhu, M., Cao, C., Xu, Z., Tsatskis, Y., Lau, K., Kuok, C., Filleter, T., McNeill, H., et al. (2018). Mechanical stability of the cell nucleus - roles played by the cytoskeleton in nuclear deformation and strain recovery. J. Cell Sci. *131*, jcs209627.

Watkins, S., Robel, S., Kimbrough, I.F., Robert, S.M., Ellis-Davies, G., and Sontheimer, H. (2014). Disruption of astrocyte-vascular coupling and the blood-brain barrier by invading glioma cells. Nat. Commun. *5*, 4196.

Woo, S.H., Ranade, S., Weyer, A.D., Dubin, A.E., Baba, Y., Qiu, Z., Petrus, M., Miyamoto, T., Reddy, K., Lumpkin, E.A., et al. (2014). Piezo2 is required for Merkel-cell mechanotransduction. Nature *509*, 622–626.

Xu, L., Nirwane, A., and Yao, Y. (2019). Basement membrane and blood-brain barrier. Stroke Vasc. Neurol. *4*, 78–82.

Yang, Z.J., Ellis, T., Markant, S.L., Read, T.A., Kessler, J.D., Bourboulas, M., Schüller, U., Machold, R., Fishell, G., Rowitch, D.H., et al. (2008). Medulloblastoma can be initiated by deletion of Patched in lineage-restricted progenitors or stem cells. Cancer Cell *14*, 135–145.

Yankaskas, C.L., Bera, K., Stoletov, K., Serra, S.A., Carrillo-Garcia, J., Tuntithavornwat, S., Mistriotis, P., Lewis, J.D., Valverde, M.A., and Konstantopoulos, K. (2021). The fluid shear stress sensor TRPM7 regulates tumor cell intravasation. Sci. Adv. *7*, eabh3457.

Yu, G., Wang, L.G., Han, Y., and He, Q.Y. (2012). clusterProfiler: an R package for comparing biological themes among gene clusters. Omics *16*, 284–287.

Zhang, L., He, X., Liu, X., Zhang, F., Huang, L.F., Potter, A.S., Xu, L., Zhou, W., Zheng, T., Luo, Z., et al. (2019a). Single-cell transcriptomics in medulloblastoma reveals tumor-initiating progenitors and oncogenic cascades during tumorigenesis and relapse. Cancer Cell *36*, 302–318.e7.

Zhang, X., Lan, Y., Xu, J., Quan, F., Zhao, E., Deng, C., Luo, T., Xu, L., Liao, G., Yan, M., et al. (2019b). CellMarker: a manually curated resource of cell markers in human and mouse. Nucleic Acids Res. *47*, D721–D728.

Zhou, T., Gao, B., Fan, Y., Liu, Y., Feng, S., Cong, Q., Zhang, X., Zhou, Y., Yadav, P.S., Lin, J., et al. (2020). Piezo1/2 mediate mechanotransduction essential for bone formation through concerted activation of NFAT-YAP1-ss-catenin. eLife *9*, e52779.

Zhou, W., Chen, C., Shi, Y., Wu, Q., Gimple, R.C., Fang, X., Huang, Z., Zhai, K., Ke, S.Q., Ping, Y.F., et al. (2017). Targeting glioma stem cell-derived pericytes disrupts the blood-tumor barrier and improves chemotherapeutic efficacy. Cell Stem Cell *21*, 591–603.e4.

STAR★METHODS

KEY RESOURCES TABLE

REAGENT or RESOURCE	SOURCE	IDENTIFIER
Antibodies		
Chicken anti-GFAP	EMD Millipore	Cat# AB5541; RRID:AB_177521
Mouse anti-GFAP	EMD Millipore	Cat# MAB360; RRID:AB_11212597
Mouse anti-Sox2	Abcam	Cat# ab79351; RRID:AB_10710406
Rabbit anti-Sox2	Abcam	Cat# ab97959; RRID:AB_2341193
Mouse anti-Dcx	Abcam	Cat# ab135349
Rabbit anti-NeuN	Abcam	Cat# ab104225; RRID:AB_10711153
Mouse anti-NeuN	EMD Millipore	Cat# MAB377; RRID:AB_2298772
Rabbit anti-Desmin	Abcam	Cat# ab32362; RRID:AB_731901
Rat anti-CD31	BD Biosciences	Cat# 550274; RRID:AB_393571
Rabbit anti-Slc2a1	EMD Millipore	Cat# 07-1401; RRID:AB_1587074
Rat anti-Plvap	Bio-Rad	Cat# MCA2539GA; RRID:AB_931734
Rabbit anti-Pdgfrβ	Abcam	Cat# ab32570; RRID:AB_777165
Rabbit anti-ColIV	Bio-Rad	Cat# 2150-1470; RRID:AB_2082660
Rabbit anti-ZO-1	Thermo Fisher Scientific	Cat# 61-7300; RRID:AB_2533938
Rabbit anti-Ki67	Abcam	Cat# ab15580; RRID:AB_443209
Mouse anti-Nestin	EMD Millipore	Cat# MAB353, RRID:AB_94911
Rabbit anti-Pax6	BioLegend	Cat# 901301; RRID:AB_2565003
Mouse anti-phospho-Histone 3	Cell Signaling Technology	Cat# 9706; RRID:AB_331748
Mouse anti-PCNA	Santa Cruz Biotechnology	Cat# sc-56; RRID:AB_628110
Rabbit anti-cleaved-Caspase-3	Cell Signaling Technology	Cat# 9661; RRID:AB_2341188
Chicken anti-GFP	Aves Labs	Cat# GFP-1010; RRID:AB_2307313
Mouse anti-GFP	Clontech	Cat# 632381; RRID:AB_2313808
Rabbit anti-tdTomato	Rockland Inc.	Cat# 600-401-379; RRID:AB_2209751
Mouse anti-STEM121	Takara Bio Inc.	Cat# Y40410; RRID:AB_2801314
Rabbit anti-Ng2	Millipore Sigma	Cat# AB5320, RRID:AB_91789
Rabbit anti-Fibrinogen	Abcam	Cat# ab34269; RRID:AB_732367
Mouse anti-β-Catenin	BD Biosciences	Cat# 610153; RRID:AB_397554
Rabbit anti-Lef1	Cell Signaling Technology	Cat# 2230; RRID:AB_823558
Rabbit anti-Pdgfb	Thermo Fisher Scientific	Cat# bs-0185R; RRID:AB_10859010
Mouse anti-phospho myosin light chain 2 (Ser19)	Cell Signaling Technology	Cat# 3675; RRID:AB_2250969
Mouse anti-P-glycoprotein	Thermo Fisher Scientific	Cat# MA1-26528; RRID:AB_795165
Rat anti-E-cadherin	Invitrogen	Cat# 14-3249-82; RRID:AB_1210458
Mouse anti-Laminin Alpha-2	Abcam	Cat# ab236762
Goat anti-Laminin Alpha-4	R&D Systems	Cat# AF3837; RRID:AB_2249744
Mouse anti-Claudin5	Invitrogen	Cat# 352588; RRID:AB_2532189
Rabbit anti-phospho myosin light chain 2 (Ser19)	Cell Signaling Technology	Cat# 3671; RRID:AB_330248
Mouse anti-RhoA-GTP	NewEast Biosciences	Cat# 26904; RRID:AB_1961799
Rabbit anti-RhoA	Cell Signaling Technology	Cat# 2117; RRID:AB_10693922
Mouse anti-Fyn	BD Biosciences	Cat# 610163; RRID:AB_397564
Rabbit anti-phospho-FAK (Tyr397)	Invitrogen	Cat# 44-624G; RRID:AB_2533701
Rabbit anti-phospho-Paxillin (Tyr118)	Invitrogen	Cat# 44-722G; RRID:AB_2533733
Mouse anti-Vinculin	EMD Millipore	Cat# MAB3574; RRID:AB_2304338
Rabbit anti-SerpinB2	Abcam	Cat# ab137588; RRID:AB_2891205

(*Continued on next page*)

Continued

REAGENT or RESOURCE	SOURCE	IDENTIFIER
Bacterial and virus strains		
pLKO.1-shPIEZO2 #1	Dharmacon	Clone ID: TRCN0000123251
pLKO.1-shPIEZO2 #2	Dharmacon	Clone ID: TRCN0000123253
pcDNA3.1^{+}-Piezo2 cDNA	GenScript	Clone ID: OMu00667
Chemicals, peptides, and recombinant proteins		
Phalloidin	Cell Signaling Technologies	Cat# 8878S
DAPI	Sigma-Aldrich	Cat# D9564
XenoLight D-Luciferin Potassium Salt	PerkinElmer Health Sciences Canada, Inc.	Cat# 122799
Sulfo SANPAH Crosslinker	Sigma Aldrich	Cat# 803332
Poly-L-ornithine solution	Sigma Aldrich	Cat# P4957
Laminin from Engelbreth-Holm-Swarm murine sarcoma basement membrane	Sigma Aldrich	Cat# L2020
NeuroCult NS-A Basal Medium (Mouse & Rat)	StemCell Technologies	Cat# 05700
Recombinant human EGF	Sigma Aldrich	Cat# E9644
Basic FGF	StemCell Technologies	Cat# 02634
B27 Supplement	GIBCO	Cat# 12-587-001
Accutase	StemCell Technologies	Cat#07920
Fluo-4 AM	Invitrogen	Cat# F14201
Fura Red	Invitrogen	Cat# F3020
Dimethyl sulfoxide	Fisher Scientific	Cat# BP231-100
Y-27632	Tocris	Cat# 1254
Calyculin A (CalyA)	Tocris	Cat# 1336
Fluospheres™ Carboxylate-Modified Microspheres	Thermo Scientific	Cat# F8810
Recombinant Human/Mouse Wnt-5a Protein	R&D Systems	Cat# 645-WN-010
Etoposide (VP-16)	Santa Cruz Biotechnology	Cat# sc-3512
Gadolinium chloride (GdCl3)	Tocris	Cat# 4741
Cadaverine-Alexa555	Invitrogen	Cat# A30677
Dextran-Alexa555	Invitrogen	Cat# D34679
Evans blue	Sigma Aldrich	Cat# E2129
polyethylene glycol 1500 (PEG1500)	Sigma-Aldrich	Cat# 10783641001
Critical commercial assays		
Trypan Blue Solution, 0.4%	ThermoFisher Scientific	Cat# 15250061
RNeasy Plus Mini Kit	Qiagen	Cat# 74134
Nucleofector Kits for Mouse Neural Stem Cells	Lonza	Cat# VVPG1004
Calpain Activity Assay Kit (ab65308)	Abcam	Cat# ab65308
SensiFAST™ cDNA Synthesis Kit	Bioline	Cat# BIO-65054
ApopTag® Fluorescein In Situ Apoptosis Detection Kit (TUNEL assay)	Sigma-Aldrich	Cat# S7110
Deposited data		
Mouse scRNAseq data	This paper	SRA: PRJNA588007 and GEO: GSE197402

(*Continued on next page*)

Continued

REAGENT or RESOURCE	SOURCE	IDENTIFIER
scRNA-seq datasets of Human MBs	Hovestadt et al., 2019; Riemondy et al., 2022	GEO: GSE119926 and GEO: GSE156053
RNA-seq or microarray data from human SHH MBs	Cavalli et al., 2017; Ramaswamy and Taylor, 2019; Suzuki et al., 2019	EGA: EGAD00001001899, EGA: EGAD00001004958, and GEO: GSE85218
Experimental models: Cell lines		
Mouse Sox2^{+} MB cells	This paper	N/A
ONS76 cell line	Laboratory of Dr. Michael D. Taylor	N/A
Human brain microvascular endothelial cells (hCMEC/D3)	Cedarlane Labs	Cat# CLU512
MDA-MB-231 cells	Gift from Drs. Joan Massagué and Adrienne Boire; Boire et al., 2017	N/A
Experimental models: Organisms/strains		
Ptch1$^{+/-}$	The Jackson Laboratory	RRID:IMSR_JAX:003081
Math1-Cre	The Jackson Laboratory	RRID:IMSR_JAX:011104
Rosa26-LSL-SmoM2-YFP	The Jackson Laboratory	RRID:IMSR_JAX:005130
Sox2^{GFP}	The Jackson Laboratory	RRID:IMSR_JAX:017592
Piezo2-EGFP-IRES-Cre (*Piezo2*$^{tm1.1(cre)Apat}$)	The Jackson Laboratory	RRID:IMSR_JAX:027719
Piezo2$^{fl/fl}$ (*Piezo2*$^{tm2.2Apat}$)	The Jackson Laboratory	RRID:IMSR_JAX:027720
Piezo1$^{P1\text{-}tdT}$ (*Piezo1*$^{tm1.1Apat}$)	The Jackson Laboratory	RRID:IMSR_JAX:029214
Piezo1$^{fl/fl}$ (*Piezo1*$^{tm2.1Apat}$)	The Jackson Laboratory	RRID:IMSR_JAX:029213
tdTomato reporter	The Jackson Laboratory	RRID:IMSR_JAX:007914
Oligonucleotides		
mPiezo2-Forward: AAGCAAACGAGAACTTTACATGG	This paper	N/A
mPiezo2-Reverse: AGCACGTATACATCAGTCACAGC	This paper	N/A
mTrpc1-Forward: GTCGCACCTGTTATTTTAGCTGC	This paper	N/A
mTrpc1-Reverse: TGGGCAAAGACACATCCTGC	This paper	N/A
mTrpv4-Forward: ATGGCAGATCCTGGTGATGG	This paper	N/A
mTrpv4-Reverse: GGAACTTCATACGCAGGTTTGG	This paper	N/A
mTrpm7-Forward: AGGATGTCAGATTTGTCAGCAAC	This paper	N/A
mTrpm7-Reverse: CCTGGTTAAAGTGTTCACCCAA	This paper	N/A
mTmem63a-Forward: GGCTGTGTTTGTCCGTGAG	This paper	N/A
mTmem63a-Reverse: GGATGCCTCCAAAGGTGACC	This paper	N/A
mGapdh-Forward: TTCACCACCATGGAGAAGGC	This paper	N/A
mGapdh-Reverse: GGCATGGACTGTGGTCATGA	This paper	N/A

(*Continued on next page*)

Continued

REAGENT or RESOURCE	SOURCE	IDENTIFIER
Recombinant DNA		
Plasmid: pLKO.1-shPIEZO2 #1	Dharmacon	Clone ID: TRCN0000123251
Plasmid: pLKO.1-shPIEZO2 #2	Dharmacon	Clone ID: TRCN0000123253
Plasmid: pcDNA3.1^{+}-Piezo2 cDNA	GenScript	Clone ID: OMu00667
Software and algorithms		
GraphPad Prism 9	GraphPad Software, Inc.	https://www.graphpad.com/scientific-software/prism/
pClamp10	Molecular Devices	https://www.moleculardevices.com/products/axon-patch-clamp-system#gref
MATLAB	The MathWorks	https://www.mathworks.com/
Image J	National Institutes of Health	https://imagej.nih.gov/ij/
Leica LAS software	Leica Microsystems	https://www.leica-microsystems.com/products/microscope-software/p/leica-las-x-ls/
Fleximaging v3.0	Bruker Corporation	https://www.directindustry.com/prod/bruker-daltonics/product-30029-1007957.html
Imaris 9.3	Oxford Instruments	https://imaris.oxinst.com/versions/9-3
MALDI: SCiLS (2015b)	Bruker Corporation	https://www.bruker.com/en/products-and-solutions/mass-spectrometry/ms-software/scils-lab.html
LC-MS/MS: XCMS	Smith et al., 2006	https://pubs.acs.org/doi/10.1021/ac051437y
Cell Ranger v 3.0	10X Genomics	https://support.10xgenomics.com/single-cell-gene-expression/software/downloads/latest
Velocyto.py v0.17	La Manno et al., 2018	http://velocyto.org/
R v3.6	The R Project	https://cran.r-project.org/bin/windows/base/old/3.6.3/
Python v3.6.3	Python Software Foundation	https://www.python.org/downloads/release/python-363/
Seurat v4.0.6	Hao et al., 2021	https://satijalab.org/seurat/
SeuratWrappers v0.3.0	The Satija Lab	https://github.com/satijalab/seurat-wrappers
Velocyto.R v0.6	La Manno et al., 2018	http://velocyto.org/
DESseq2 v1.26.0	Love et al., 2014	https://bioconductor.org/packages/release/bioc/html/DESeq2.html
ClusterProfiler v3.14.3	Yu et al., 2012	https://bioconductor.org/packages/release/bioc/html/clusterProfiler.html
biomaRt v2.50	Durinck et al., 2009	https://bioconductor.org/packages/release/bioc/html/biomaRt.html
AUCell v1.16.0	Aibar et al., 2017	https://www.bioconductor.org/packages/release/bioc/html/AUCell.html
Biobase v2.54.0	Huber et al., 2015	https://bioconductor.org/packages/release/bioc/html/Biobase.html
BiocGenerics v0.40.0	Huber et al., 2015	https://bioconductor.org/packages/release/bioc/html/BiocGenerics.html
survival v3.2.13	The R Project	https://cran.r-project.org/web/packages/survival/index.html
Dynverse (dyno v0.1.2, dynwrap v1.2.2, dynmethods v1.0.5, dynguidelines v1.0.1, dynfeature v1.0.0)	Saelens et al., 2019	https://dynverse.org/

RESOURCE AVAILABILITY

Lead contact

Further information and requests for reagents should be directed to and will be fulfilled by the lead contact, Xi Huang (xi.huang@sickkids.ca).

Materials availability

Reagents generated in this study are available from the lead contact with a completed Materials Transfer Agreement.

Data and code availability

Raw scRNA-seq data of mouse medulloblastoma have been deposited at Sequence Read Archive (SRA) and Gene Expression Omnibus (GEO). They are publicly available at the date of publication. The accession numbers are listed in key resources table.

This paper analyzed publicly available scRNA-seq, bulk RNA-seq, and microarray datasets of human medulloblastoma, which were downloaded from GEO and European Genome-phenome Archive (EGA). These accession numbers are listed in key resources table.

This paper does not report original code.

Any additional information required to reanalyze the data reported in this paper is available from the lead contact upon request.

EXPERIMENTAL MODEL AND SUBJECT DETAILS

Mouse

Ptch1$^{+/-}$ (Goodrich et al., 1997), *Math1-Cre* (Yang et al., 2008), *Rosa26-LSL-SmoM2-YFP* (Ligon et al., 2007), *Sox2-GFP (B6;129S-Sox2tm2Hoch/J)* (Arnold et al., 2011), *Piezo2-EGFP-IRES-Cre* (*Piezo2*$^{tm1.1(cre)Apat}$) (Woo et al., 2014), *Piezo2*$^{fl/fl}$ (*Piezo2*$^{tm2.2Apat}$) (Woo et al., 2014), *Piezo1*$^{P1\text{-}tdT}$ (*Piezo1*$^{tm1.1Apat}$) (Ranade et al., 2014a), *Piezo1*$^{fl/fl}$ (*Piezo1*$^{tm2.1Apat}$) (Cahalan et al., 2015) mice were previously described. *Math1-Cre; SmoM2* mice develop SHH MB due to hyperactive SHH signaling induced by SmoM2 (the constitutively active form of SHH pathway receptor Smo) in cerebellar granule neuron precursors (CGNPs), achieved by CGNP-specific driver *Math1-Cre* (Schüller et al., 2008; Yang et al., 2008). *Ptch1*$^{+/-}$ mice develop SHH MB due to loss of one allele of SHH pathway inhibitor *Ptch1* and subsequent loss-of-heterozygosity (Goodrich et al., 1997), which drives constitutive SHH signaling in CGNPs. We crossed *Math1-Cre* mice with *Ai14* reporter mice (Jax strain:007914) to drive the expression of tdTomato in Math1-lineage cells. For xenograft mice, Med813FH (SHH-MB-1, SHH MB from a 2-year-old male, purchased from Brain tumour Resource Laboratory), and ONS76 cell lines (Garzia et al., 2018) were used. Xenograft procedures were previously described (Donovan et al., 2020; Francisco et al., 2020). For genetically engineered mouse models, both sexes were included in the study. For xenograft experiments, 8-week old female *NOD scid gamma/J#5557* immunodeficient mice were used. Mouse age is specified in the figures or text. Most mice from genetically engineered models were studied before reaching sexual maturity (at P21 or earlier). The influence of sex was not evaluated in this study.

For survival analysis, mice were either intraperitoneally injected with vehicle or etoposide (Santa Cruz, sc-3512A) at 30 μg/10 g daily beginning at P18. For MALDI imaging mass spectrometry, mice were intraperitoneally injected with vehicle or etoposide at 30 μg/10 g at P21. Two hours after injection, mice were euthanized. MB tissues were snap-frozen on an aluminum boat in liquid nitrogen for 5 minutes, stored at -80 C°, and processed for experiments. For immunohistochemistry after chemotherapy, P18 mice or xenograft mice were intraperitoneally injected with vehicle or etoposide at 30 μg/10 g for 5 consecutive days. The brains were collected at P23. To quantify the weight ratio of MB to the whole brain, P18 mice were intraperitoneally injected with vehicle or etoposide at 30 μg/10 g for 6 consecutive days. The brains were weighted at P24. Mice were maintained in specific pathogen-free conditions in the animal facility with 12:12 h light/dark cycles. Our mouse protocol (19-0288H) was approved by The Centre for Phenogenomics (TCP) Animal Care Committee. All mouse procedures were performed in compliance with Animals for Research Act of Ontario and the Guidelines of Canadian Council on Animal Care.

Cell cultures

Mouse Sox2^{+} MB cells were isolated from primary tumors of P21 control (*Math1-Cre; SmoM2*) and Piezo2 knockout (*Math1-Cre; SmoM2; Piezo2*$^{fl/fl}$) mice and cultured as previously described (Huang et al., 2010). Briefly, MB were dissociated by repetitive pipetting using ice-cold PBS without Mg^{2+} and Ca^{2+}, followed by treatment using 50% Accutase diluted in PBS. The dissociated cells were cultured on plates coated with poly-L-ornithine and laminin, using Neurocult NS-A Basal media (Mouse & Rat) supplemented with 2 mM L-glutamine, 1x B27-A (Gibco), 1x hormone mix (in-house N2 supplement), 75 μg/mL BSA, 20 ng/ml human rhEGF (STEMCELL Technologies), 20 ng/ml human bFGF (STEMCELL Technologies), and 2 μg/mL heparin (Sigma-Aldrich). Half of the media were replaced by fresh media every 3 days. MDA-MB-231 cells are Gift from Drs. Joan Massagué and Adrienne Boire. Cells were cultured in Dulbecco's Modified Eagle Medium (DMEM) supplemented with 10% fetal bovine serum (FBS). Human brain microvascular endothelial cells (hCMEC/D3) were purchased from Cedarlane Labs (Cat. #CLU512) and cultured according to the company data sheet.

METHOD DETAILS

Immunohistochemistry and image quantifications

Immunohistochemistry and hematoxylin and eosin (H&E) staining were performed on CRYO- or paraffin-embedded tissue sections. For xenograft tumors, Med813FH (SHH MB from a 2-year-old male, purchased from Brain tumour Resource Laboratory), and ONS76 cell lines (Garzia et al., 2018) were used. Xenograft procedures were previously described (Donovan et al., 2020; Francisco et al., 2020).

Primary antibodies were Anti-GFAP (1:200, AB5541, EMD Millipore), Anti-GFAP (1:200, MAB360, EMD Millipore), Anti-Sox2 (1:100, ab79351, Abcam), Anti-Sox2 (1:100, ab97959, Abcam), Anti-Dcx (1:100, ab18723, Abcam), Anti-Dcx (1:100, ab135349, Abcam), Anti-NeuN (1:100, ab104225, Abcam), Anti-NeuN (1:100, MAB377, EMD Millipore), Anti-Desmin (1:100, ab32362, Abcam), Anti-CD31 (1:100, 550274, BD Biosciences), Anti-Slc2a1 (1:100, 07-1401, EMD Millipore), Anti-Plvap (1:100, MCA2539GA, Bio-Rad), Anti-Pdgfrβ (1:100, ab32570, Abcam), Anti-ColIV (1:200, 2150-1470, Bio-Rad), Anti-ZO-1 (1:100, 61-7300, Thermo Fisher Scientific), Anti-Ki67 (1:100, ab15580, Abcam), Anti-Nestin (1:100, MAB353, EMD Millipore), Anti-Pax6 (1:100, 901301, BioLegend), Anti-phospho-Histone 3 (1:100, 9706, Cell Signaling), Anti-PCNA (1:100, sc56, Santa Cruz Biotechnology), Anti-cleaved-Caspase-3 (1:100, 9661S, Cell Signaling Technology), Anti-GFP (1:100, AB2307313, Aves Labs), Anti-GFP (1:100, 632381, Clontech), Anti-tdTomato (1:100, 600-401-379, Rockland Inc.), Anti-STEM121 (1:100, Y40410, Takara Bio Inc.), Anti-Ng2 (1: 200, AB5320, Millipore Sigma), Anti-Fibrinogen (1:100, ab34269, Abcam), Anti-β-catenin (1:100, 610153, BD Biosciences), Anti-Lef1 (1:100, #C12A5, Cell Signaling Technology), Anti-Pdgfb (1:100, BS-0185R, Thermo Fisher Scientific), Anti-phospho myosin light chain 2(Ser19) (1:100,3675S, Cell Signaling Technology), Anti-P-glycoprotein (1;100,MA126528, Thermo Scientific), Anti-E-cadherin (1;100,14-3249-82, Invitrogen), Anti-Laminin Alpha-2 (1:100, ab236762, Abcam), Anti-Laminin Alpha-4 (1:100, AF3837, R&D Systems), and Anti-Claudin5 (1:100, 352588, Invitrogen). Secondary antibodies conjugated to Alexa-Fluor dyes (488, 555, 647) at a dilution of 1:200 were used. TUNEL kit (Cat. #S7110, Sigma-Aldrich) was used for apoptosis. DAPI (Cat. #D9564, Sigma-Aldrich) was used for nuclear counterstain.

All images were acquired using a Leica SP8 confocal microscope. All images were 3D reconstructed and analyzed using the software Imaris. Image quantification methods are described below.

The number, endfeet width, and length of GFAP$^+$ cells

Cellular branches were identified in 3D images. The number of branches that stem from GFAP$^+$ cell body were recorded. Branch length was defined as the total distance between cell body and ending of individual branches. Endfeet width was determined as GFAP$^+$ surface on endothelial cells. Measurements were performed using Imaris 3D measurement tool "Type Polygon", which traces the distance of a 3D pathway between the first and last manually defined points.

Capillary coverage by GFAP$^+$ cells

CD31$^+$ signal was determined by the "Surface" function. Using the "mask channel" function, we created a surface mask for GFAP$^+$ signal that contacts CD31$^+$ signal. CD31$^+$ signal in contact with GFAP$^+$ signal was divided by total CD31$^+$ signal to determine the extent of capillary coverage by GFAP$^+$ cells.

Pericyte coverage

CD31$^+$ signal was determined by the "Surface" function. Using the "mask channel" function, we created a surface mask for Pdgfrβ$^+$ signal that contacts CD31$^+$ signal. CD31$^+$ signal in contact with Pdgfrβ$^+$ signal was divided by total CD31$^+$ signal to determine the extent of capillary coverage by Pdgfrβ$^+$ pericytes.

ColIV, Lama2, Lama4, and Claudin5 expression

CD31$^+$ signal was determined by the "Surface" function. Mean ColIV$^+$, Lama2$^+$, Lama4$^+$, and Claudin5$^+$ signal intensity was determined in capillaries.

ZO-1 expression

CD31$^+$ signal was determined by the "Surface" function. Using the "mask channel" function, the overlap of CD31$^+$ and ZO-1$^+$ signals was determined. CD31$^+$; ZO-1$^+$ signal was divided by total CD31$^+$ signal to determine relative ZO-1 expression in capillaries.

Plvap and Slc2a1 expression

Plvap$^+$ signal was determined by the "Surface" function. The ratio of Plvap$^+$ signal to Slc2a1$^+$; Plvap$^+$ signal was determined in capillaries.

Capillary number, diameter, and density

Total numbers of capillaries were manually counted. An average value was calculated across z-stacks. "IsoSurface" function in Imaris was used with smoothing level of 0.5 μm and uniform background subtraction. Manual thresholding of "surface mask" was determined using "IsoSurface". These procedures optimized the reconstruction of CD31$^+$ blood vessels. To determine vessel diameter, images were rotated such that the cross-section of the vessel became parallel to the x-y axis. Vessel diameter and length were determined using the "Type Polygon" function. Vessel volume was determined using "IsoSurface". Vascular density was defined as length/volume.

Capillary coverage by Sox2-eGFP$^+$ cells

CD31$^+$ signal was determined using the "Surface" function. Using the "mask channel" function, CD31$^+$; Sox2-eGFP$^+$ signal was measured and divided by total CD31$^+$ signal to determine the extent of capillary covered by Sox2-eGFP$^+$ cells.

Proportion of neoplastic Sox2$^+$ and Ki67$^+$ cells

The "Spots" function was used to identify Sox2$^+$ cells. Using the "mask channel" function, Sox2$^+$ and SmoM2-eYFP$^+$ signal overlap was determined. Sox2$^+$; SmoM2-eYFP$^+$ spot number was divided by total Sox2$^+$ spot number to determine the proportion of neoplastic (SmoM2-eYFP$^+$) Sox2$^+$ cells. This quantification method was also used to determine the proportion of neoplastic Ki67$^+$ cells.

Proportion of neoplastic GFAP$^+$, Desmin$^+$, AQP4$^+$, and Pdgfrβ^+ cells

Cells with GFAP$^+$, Desmin$^+$, AQP4$^+$, or Pdgfrβ^+ cell body or processes that overlap with SmoM2-eYFP$^+$ signal were determined. The number of double positive cells was divided by total SmoM2-eYFP$^+$ cells to determine which cell types are neoplastic.

Proportion of GFAP$^+$, Desmin$^+$, and Aldh1l1$^+$ cells expressing Piezo2

Cells with GFAP$^+$, Desmin$^+$, AQP4$^+$, or Pdgfrβ^+ cell body or processes that overlap with Piezo2-eGFP$^+$ signal were determined. The number of double positive cells was divided by total Piezo2-eYFP$^+$ cells to determine which cell types express Piezo2.

Fibrinogen/Cadaverine/Dextran/Evans blue experiment

Fibrinogen$^+$/Cadaverine$^+$/Evans blue$^+$ signal was determined using the "Surface" function. Tumor volume was determined by DAPI$^+$ signal. Fibrinogen$^+$/Cadaverine$^+$/Evans blue$^+$ signal was divided by total DAPI$^+$ signal to determine Fibrinogen distribution in MB.

GFAP$^+$ cell coverage on ColIV, Pdgfrβ, and ZO-1 signal

ColIV$^+$ signal was determined using the "Surface" function. Using the "mask channel" function, ColIV$^+$ and GFAP$^+$ signal overlap was determined. ColIV$^+$; GFAP$^+$ signal was divided by total ColIV$^+$ signal to determine the extent of GFAP$^+$ cell coverage on vascular basement membrane. Similar procedure was used to determine GFAP$^+$ cell coverage on Pdgfrβ^+ pericytes and ZO-1$^+$ endothelium.

Proportion of cycling Sox2$^+$ cells

Using the "Spots" function, proportion of cycling Sox2$^+$ cells were determined by quantifying the number of Sox2$^+$ cells which are Ki67$^+$ within the total population of Sox2$^+$ cells. Sox2$^+$; Ki67$^+$ cells were defined as cells with an overlap of greater than 50% of Sox2$^+$ signal over Ki67$^+$ signal in 3D.

Endothelial cell surface area to volume ratio

CD31$^+$ signal was determined using the "Surface" function. Using 3D reconstruction, surface area and volume for CD31$^+$ per frame were determined.

Measurements of the numbers and immunostaining signal colocalization of other cell types

Using the "Spots" function, the numbers of Sox2$^+$, PCNA$^+$, Sox2-eGFP$^+$, NeuN$^+$, pHis3$^+$, TUNEL$^+$, β-Catenin$^+$, cleaved-Caspase-3$^+$ cells in relation with other immunostained markers were quantified. Signal colocalization was determined using similar procedures described in "Proportion of cycling Sox2 cells" (for nuclear signals), "Proportion of neoplastic GFAP$^+$, Desmin$^+$, and Pdgfrβ^+ cells" (for cytoplasmic signals), and "Proportion of neoplastic Sox2$^+$ cells" (for nuclear and cytoplasmic signals). Percent of β-Catenin$^+$ or Lef1$^+$ endothelial cells were quantified as CD31$^+$ endothelial cells with β-Catenin or Lef1 immunostaining signal in nuclei within total endothelial cells. Pdgfrβ^+ signal was determined using the "Surface" function. Using the "mask channel" function, pMLC2$^+$ and Pdgfrβ^+ signal overlap that covers capillaries was determined. pMLC2$^+$; Pdgfrβ^+ signal was divided by Pdgfrβ^+ signal that covers capillaries to determine the percent of pMLC2$^+$ pericytes. Similar procedure was used to determine β-Catenin$^+$ signal in the processes or soma of GFAP$^+$ cells, and to determine β-Catenin$^+$ distal processes in total processes adjacent to capillaries by restricting the measurement at the area of GFAP$^+$ processes adjacent to CD31$^+$ endothelial cells. Relative Pdgfb level in Sox2$^+$ MB cells was determined using a similar procedure by quantifying Pdgfb$^+$; GFAP$^+$ signal divided by total GFAP$^+$ signal in the images.

Capillary coverage by human MB cells

To determine capillary coverage by STEM121$^+$ human MB cells, CD31$^+$ signal was determined using the "Surface" function. Using the "mask channel" function, CD31$^+$ and STEM121$^+$ signal overlap was determined. CD31$^+$; STEM121$^+$ signal was divided by total CD31$^+$ signal to determine the extent of capillary coverage by human MB cells.

Desmin$^+$ signal overlap with Pdgfrβ^+ signal

Desmin $^+$ signal was determined using the "Surface" function. Using the "mask channel" function, Desmin $^+$ and Pdgfrβ $^+$ signal overlap was determined. Desmin$^+$; Pdgfrβ^+ signal was divided by total Desmin$^+$ signal to determine the extent of Desmin$^+$ signal overlap with Pdgfrβ^+ pericytes.

Endothelial cell volume and aspect ratio measurement

As a transmembrane glycoprotein continuously present on the cell surface, CD31 demarcates the periphery of endothelial cells. We determined endothelial cell morphology using CD31 signals that are in contact with the DAPI$^+$ endothelial cell nucleus. Representative 3D reconstructions of endothelial cell morphology and nucleus of control and Piezo2 knockout MB are shown in Figure S6G. After 3D reconstruction, "IsoSurface" function of Imaris was used to determine the cell or nuclear volume. "Type Polygon" function of Imaris was used to determine the length and width of cell or nucleus. Aspect ratio was defined as the ratio of length / width.

Transmission electron microscopy (TEM)

Mice were anaesthetized, perfused with PBS followed by EM grade fixative (4% paraformaldehyde and 2.5% glutaraldehyde in 0.1 M cacodylate buffer). MB were harvested and fixed by immersion in the fixative overnight at 4 °C. Tissues were rinsed in cacodylate buffer, post-fixed in 1% osmium tetroxide in buffer, dehydrated in a graded ethanol series (50%, 70%, 90% and 100%) followed by propylene oxide, and embedded in Quetol-Spurr resin. 70 nm thick sections were cut using a Leica EM UC7 ultramicrotome, stained with uranyl acetate and lead citrate, and viewed using a FEI Tecnai 20 TEM at 120 kV. The thickness of basement membrane

for each image was measured using ImageJ in 5 random regions each containing an endothelial cell. By adopting a published method (O'Brown et al., 2019), the density of luminal and abluminal vesicles in endothelial cells were defined as the number of vesicles per μm perimeter of the luminal or abluminal membrane of endothelial cells using ImageJ. Abnormal tight junctions are defined as tight junctions with widened space or lacking electron-dense structures between adjoining endothelial cells.

Hypertonicity and hypotonicity treatment to endothelial cells

Human brain microvascular endothelial cells (hCMEC/D3) were purchased from Cedarlane Labs (Cat. #CLU512) and cultured according to the company data sheet. Hypertonicity treatment was performed by adding polyethylene glycol 1500 (PEG1500) (Cat. #10783641001, Sigma-Aldrich) to cell culture medium (Li et al., 2020, 2021). Hypotonicity treatment was performed by adding Milli-Q water to achieve 75% medium (Li et al., 2020, 2021). After 24-hour treatment, cells were fixed using 4% formaldehyde at room temperature 20 minutes and incubated with primary antibody including Anti-β-CATENIN (610153, BD Biosciences) and Anti-LEF1 (#C12A5, Cell Signaling Technology) at 4 °C overnight and secondary antibody at room temperature for 1 hour. Images were analyzed using the "Surface" function of Imaris to obtain relative fluorescence intensity of β-CATENIN and LEF1 per nucleus (the mask was generated based on DAPI staining).

Generating coverslips with various levels of substrate stiffness

Polyacrylamide gel substrate with 1k and 5k stiffness were fabricated on glass coverslips. Polyacrylamide gel solutions were prepared by mixing acrylamide (5%, Bio-Rad) and bis-acrylamide (0.03% or 0.14%, Bio-Rad) in deionized water. Polymerization was initiated with 0.05% ammonium persulfate (Sigma) and 0.1% N,N,N',N'-Tetramethylethylenediamine (TEMED, Sigma). 15 μl of each solution was pipetted onto glass coverslips treated with 0.5% 3-aminopropyltrimethoxysilane (Sigma) and 1% glutaraldehyde (Sigma). To cross-link extracellular matrix protein onto polyacrylamide gel surface, the gels were photoactivated by sulfo-SANPAH (Sigma) under UV light for 8 minutes. Subsequently, gels were sterilized with peracetic acid for 10 minutes, washed well, then incubated in 200 μg/mL laminin solution (Sigma) at 37°C overnight. The Young's modulus (1 kPa or 5 kPa) of polyacrylamide gels was confirmed by atomic force microscopy.

Applying axial compression using a compressive load system

To apply compressive stress on cells, different weights (0.09–0.45 g) were put on a coverslip mounted on the cells. The magnitude of force/cell was calculated considering total area of the coverslip, number of cells seeded, and weight applied on the coverslip (Kumar et al., 2014). After 1 hour of static compressive stress, cells were fixed using 4% formaldehyde at room temperature for 20 minutes, incubated with primary antibody including Anti-β-CATENIN (610153, BD Biosciences) and Anti-LEF1 (C12A5, Cell Signaling Technology) at 4 °C overnight, and secondary antibody at room temperature for 1 hour. Images were analyzed using the software Imaris functions of "Surface" to obtain mean β-CATENIN and LEF1 volume per nucleus (mask was generated based on the DAPI staining), and mean cell volume (quantified based on DAPI and β-CATENIN staining).

$$\text{Force/cell} = \text{Pressure exerted by the coverslip} \times \text{Total area of cells N/Total number of cells under coverslip}$$

$$\text{Pressure exerted by the coverslip} = \text{Coverslip weight} \times 9.8\ \text{N/kg/Area of coverslip}$$

Mouse Sox2$^+$ MB cell isolation, culture, and immunocytochemistry

Mouse Sox2$^+$ MB cells were isolated and cultured as previously described (Huang et al., 2010). Briefly, MB were dissociated by repetitive pipetting using ice-cold PBS without Mg^{2+} and Ca^{2+}, followed by treatment using 50% Accutase diluted in PBS. The dissociated cells were cultured on plates coated with poly-L-ornithine and laminin, using Neurocult NS-A Basal media (Mouse & Rat) supplemented with 2 mM L-glutamine, 1x B27-A (Gibco), 1x hormone mix (in-house N2 supplement), 75 μg/mL BSA, 20 ng/ml human rhEGF (STEMCELL Technologies), 20 ng/ml human bFGF (STEMCELL Technologies), and 2 μg/mL heparin (Sigma-Aldrich). Half of the media were replaced by fresh media every 3 days.

For cell counting, cells were plated at a density of 1000 cells per well in poly-L-ornithine- and laminin-coated 12 well plates. At 2, 4, or 6 days after seeding, cells were resuspended using Accutase (Cat. #07920, Stemcell Technologies) and incubated in isotonic solution. Cell count was acquired using Multisizer 4 Coulter Counter (Beckman-Coulter) with threshold at 10-30 μm.

For immunocytochemistry, cells were cultured on 12 mm diameter coverslips placed in 12-well plates. Cells were cultured on 5K polyacrylamide gel for at least 3 days, followed by treatment with various experimental conditions, including 10 μM Y-27632 or vehicle for 3 days, 0.3nM CalyA or vehicle for 3 days, 25 μg/ml etoposide or DMSO for 24 hours, or 0.5 μg/ml Wnt5a or vehicle for 2 days. Cells were fixed using 4% formaldehyde at room temperature 20 min, incubated with primary antibody at 4 °C overnight, and secondary antibody at room temperature for 1 hour. Primary antibodies were Anti-phospho myosin light chain 2(Ser19) (1:50,3671S, Cell Signaling Technology), Anti-RhoA-GTP (1:500, 26904, NewEast Biosciences), Anti-RhoA (1:500, 2117S, Cell Signaling Technology), Anti-Fyn(1:50, 610163, BD), Anti-phospho-FAK(Tyr397) (1:200, 44-624G, Invitrogen), Anti-phospho-Paxillin(Tyr118) (1:500, 44-722G, Invitrogen), Anti-Vinculin (1:500, MAB3574, EMD Millipore), Anti-E-cadherin (1:100,14-3249-82,

Invitrogen), Anti-β-catenin (1:1000, 610153, BD Biosciences), and Anti-Ki67 (1:1000, ab15580, Abcam). Secondary antibody was used at 1:400 dilution. Phalloidin (1:100, 8878S, Cell Signaling Technologies) was used for F-actin staining. TUNEL kit (Cat. #S7110, Sigma-Aldrich) was used to determine apoptosis. Images were acquired using Leica SP8 confocal microscope. Images were analyzed using the software Imaris functions of "Spots" (for cell number percentage), "Surface" (for intensity and size), "Surface" and "mask channel" for co-localization, "Type Polygon" for stress fiber thickness, and Image J plugins of "OrientationJ Measure" for stress fiber orientation. Co-localization of β-Catenin and E-cadherin were measured with "Surface" and "mask channel" functions in cellular process contacting sites.

Traction force microscopy

Polyacrylamide gel substrate covalently attached to coverslips were used for traction force microscopy. 5k PA gels were prepared with fluorescent bead solution (15μl/ ml; 0.2 μm in diameter; fluorescence: λex ~575 nm, λem ~610 nm; Sigma) in deionized water. Cells were cultured on polyacrylamide gels for at least 3 days. Images were captured using Leica SP8 confocal microscope with 60x oil immersion objective. Before imaging, polyacrylamide gel coverslips were mounted in a perfusion chamber and immersed with cell culture medium. For each subcellular region, images of fluorescent beads at the top surface of polyacrylamide gel were obtained while the cell were attached to the substrate. Next, 0.05% trypsin was used to detach cells followed by imaging the beads at the original subcellular region. The displacement vectors generated by cell traction force were calculated by particle imaging velocimetry (PIV) implemented as an ImageJ plugin. Based on displacement field and substrate elastic modulus, the magnitudes and directions of cell traction force were determined by Fourier-Transform Traction Cytometry (FTTC)2 and plotted by MATLAB (MathWorks Inc.).

Ratiometric calcium imaging

MB cells cultured using 5k Pa polyacrylamide gel were incubated with cell-permeant Fluo-4 AM (5 μM in DMSO, F14201, Invitrogen) and Fura Red (5 μM in DMSO, F3020, Invitrogen) for 40 minutes. After 3 times of PBS washes, the cells were incubated with culture medium for 30 minutes to allow complete de-esterification of intracellular AM esters. The culture medium was then changed to extracellular neuronal batch solution (pH 7.40 and 303 mOsm, consisted of: 140 mM NaCl, 5 mM KCl, 2 mM $CaCl_2$, 2 mM $MgCl_2$, 10 mM HEPES, and 10 mM glucose) for imaging. 3D images of the cells were captured using Leica confocal microscope with 60X objective lens, with fluorescent excitation channels at DAPI, 488 nm, and 555 nm. Excitation from 488 nm and 555 nm lasers emit Fluo-4 and Fura Red signals, respectively. Calcium level was determined by dividing Fluo-4 intensity by Fura Red intensity. Distal processes were defined as one-third of the process from the distal end. Image calculation was performed using ImageJ and MATLAB 2016.

RNA extraction, reverse transcription, and real-time RT-PCR

Total RNA from tissues or cells were extracted using TRIzol (Thermofisher) and cleaned up with a RNeasy Plus Mini kit (Qiagen). 150 ng - 1 μg RNA was reverse transcribed to cDNA using SensiFAST cDNA synthesis kit (BIOLINE). DNA and RNA concentrations were measured by a NanoDrop 1000 Spectrophotometer. Real-time detection and quantification of cDNAs were performed with the Viia7 Cycler (Applied Biosystems). qPCR was performed in a 12 μl reaction mixture using SYBR Green qPCR Supermixes (Applied Biosystems). 40 cycles of amplification were performed. Fluorescence data were collected at annealing stages and real-time analysis was performed using Viia7 System Software. Ct values were determined with automatically set baseline and manually adjusted fluorescence threshold. Gene expressions were normalized with housekeeping gene and analyzed using the ΔΔCt method.

The Primers used for qPCR are:

mouse *Piezo2* (F: AAGCAAACGAGAACTTTACATGG; R: AGCACGTATACATCAGTCACAGC);
mouse *Trpc1* (F: GTCGCACCTGTTATTTTAGCTGC; R: TGGGCAAAGACACATCCTGC);
mouse *Trpv4* (F: ATGGCAGATCCTGGTGATGG; R: GGAACTTCATACGCAGGTTTGG);
mouse *Trpm7* (F: AGGATGTCAGATTTGTCAGCAAC; R: CCTGGTTAAAGTGTTCACCCAA);
mouse *Tmem63a* (F: GGCTGTGTTTGTCCGTGAG; R: GGATGCCTCCAAAGGTGACC);
mouse *Gapdh* (F: TTCACCACCATGGAGAAGGC; R: GGCATGGACTGTGGTCATGA).

For Wnt5a experiment, total RNA was extracted from cells after 24 hours treatment. The Primers used for qPCR are: mouse *Axin2* (F: GGACTGGGGAGCCTAAAGGT; R: AAGGAGGGACTCCATCTACGC);

Electrophysiology

Mouse $Sox2^+$ MB cells were isolated from primary tumors of control (*Math1-Cre; SmoM2*) and Piezo2 knockout (*Math1-Cre; SmoM2; Piezo2*$^{fl/fl}$) mice. Cells were cultured on laminin-coated plastic coverslips for 48-72 hours. $Sox2^+$ MB cells with Piezo2 knockout were transfected with mouse Piezo2 cDNA in $pcDNA3.1^+$ (clone ID: OMu00667, purchased from GenScript, verified by sequencing) (0.25 μg per $1X10^5$ cells) with 0.025 μg GFP-encoding plasmid using the Amaxa Nucleofector Kit. Whole-cell currents were acquired from cells 40-72 hours post transfection. GFP^+ cells were selected for recording. Coverslips were transferred to a recording chamber filled with bath solution. The bath solution consisted of (in mM) 140 NaCl, 5 KCl, 1.2 CaCl2, 0.5 MgCl2, 5 glucose, and 10 HEPES (pH adjusted to 7.3 with NaOH). Patch pipettes for recording, with resistance of 3-4 MΩ, were filled with intracellular solution consisting of (in mM) 140 CsCl, 1 EGTA, 10 HEPES, 4 ATP, and 0.1 GTP (pH adjusted to 7.3 with CsOH). Whole-cell currents at -80 mV were

recorded using an Axopatch 700B amplifier (Molecular Devices). Pipettes for focal mechanical stimulation, with resistance of around 0.9-1 MΩ, were filled with the bath solution jetting stream onto the processes of $Sox2^+$ MB cells. 100 mmHg positive pressure with 100 ms duration was applied to the stimulation electrode using Clampex-controlled high-speed pressure clamp system (HSPC-1; ALA-Scientific). We developed an approach whereby mechanical stimulations can precisely target cellular processes or cell soma. We developed this approach because we found that brain cancer cells display mechanosensitivity that is highly locoregional. We showed that force application at the cellular processes, but not soma, of glioblastoma cells evoked mechanosensitive ion channel activity mediated by focal adhesion-localized PIEZO1 (Chen et al., 2018). Therefore, we adopted the same method for $Sox2^+$ MB cells. The stimulation pipette was placed within 10 μm from the cell. Cell-to-cell variability was observed in the delay from the time point when the pressure steps were commended to the time point when $Sox2^+$ cell began or stopped experiencing the solution pressure for channels activation and inactivation. All experiments were performed at room temperature. Data were acquired online, filtered at 4 kHz, digitized at 50 kHz, and analyzed offline using pClamp10 (Molecular Devices). Leak currents before mechanical stimulations were subtracted off-line. Peak current traces with fast activating and inactivating properties were calculated during the stimulating period. Data were quantified and graphed using GraphPad Prism.

Tissue stiffness measurement by 3D magnetic tweezer system

To measure tissue stiffness, we developed a single-pole magnetic tweezer system, which generates a magnetic field to mobilize fluorescent magnetic beads that were injected into fresh MB. The single-pole magnetic tweezer consists of a cone-shaped magnetic pole (iron) with a sharp tip (diameter: 21.23 μm) and 40 turns of coils (Magnetic Wire, gauge 14, Digi-Key). The magnetic tweezer was mounted on a robotic micromanipulator with a positioning accuracy of 0.2 μm in XYZ axes. The magnetic tweezer was powered by a function generator with a static currency of 2 A. To calibrate the magnetic force, the magnetic beads which were dispersed in silicone oil (AMETEK Brookfield) of known viscosities (5 mPa·s and 10 mPa·s) were actuated to move throughout the workspace by the magnetic tweezer. The navigation speed of each bead was recorded at 100 frames per second. Force exerted on the beads was calculated using the Stokes drag equation $F=6\pi R\eta v$, where R is the bead radius, η is the viscosity of the silicone oil, and v is the bead velocity calculated from the captured videos. Using live imaging, the extent of magnetic force-induced bead displacement was captured and used to calculate tissue stiffness at distinct geometrical locations within the tumor.

The magnetic bead solution (diameter: 3 μm) of 10 μL was injected into freshly harvested MB using a micropipette (tip diameter: 30 μm) under microscopic imaging. Then the MB was cut into tissue slices with thickness of 500-1000 μm. After the beads were passively diffused within the tissue for 20 minutes, a magnetic field was applied for 60 seconds, while the displacements of magnetic beads were recorded at x20 magnification (0.32 μm/pixel resolution, 100 frames per second). To compensate tissue drift, bead displacement was calculated as d = dbead – dref, where dref is the moving distance of reference point (including tissue drift), and dbead is the moving distance of beads (including tissue drift). Using bead displacement and calibrated magnetic force, the Zener model was employed to calculate tissue stiffness.

Cell stretching and calcium imaging

Cell stretching device fabrication and calibration

The 3D cell stretching microdevice array consists of three suspended PDMS membranes fabricated on a glass substrate. The fabrication process includes the following steps: (1) micromilling was used to fabricate an aluminum mold with circular pillar arrays (6.35 mm in diameter and 500 μm in height) connected by a microchannel; (2) PDMS was mixed at a 10:1 ratio of base polymer and curing agent, degassed in vacuum for 15 minutes, poured into the aluminum mold, and baked at 80 °C for 4 hours; (3) after cooling to room temperature, the PDMS base structure was peeled off and bonded to a clean glass slide by treating with oxygen plasma for 40 seconds (Harrik Plasma Cleaner PDC-001); (4) devices were biopsy punched at the microchannel inlet. Plastic tubing was applied to connect the microchannel network to a regulated pneumatic pump; (5) to form a culture chamber on each suspended membrane, three custom-made glass cylinders were bonded onto each device array by uncured PDMS and baked overnight at 80 °C. Before cell stretching, the chamber underneath the suspended membrane was filled with pre-warmed PBS to optimize imaging quality. As PBS is incompressible under pneumatic pressure, the filled PBS does not affect the pressure exerted to the suspended membrane. As we previously reported (Liu et al., 2018), the mechanical properties of PDMS membrane were calibrated through tensile testing. The strain magnitude generated on the device was calculated using Finite Element Analysis.

Quantification of intracellular calcium change

Fluo-4 (F14201, Thermo Scientific, USA) was used to measure intracellular calcium dynamics. Briefly, cells were seeded on poly-D-lysine-coated membrane of the cell stretching device for 48 hours, followed by incubation with 3 μM Fluo-4 for 30 minutes at 37°C. Cells were then washed by culture medium followed by 30 minutes incubation to allow de-esterification of intracellular AM esters. Fluo-4 signal was measured using live cell imaging solution (A14291DJ, Thermo Scientific, USA). Cyclic pressure was applied using a pneumatic pump to generate 0% and 25% mechanical strain (15 seconds per cycle) on the PDMS membrane, exerting radial tensile stress to the cells. Fluo-4 signal was determined when the mechanical strain is 0% at every cycle. Fluo-4 signal was normalized by initial intensity before stimulation. Fura Red (F3021, Thermo Scientific, USA) signal was used as calcium-independent internal control and used for further normalization of Fluo-4 signal. Fluorescence signal quantifications were performed using ImageJ. For applying a broad-spectrum blocker of mechanosensitive ion channels, $Sox2^+$ MB cells were pre-treated with 30 μM $GdCl_3$.

Calpain activity

The calpain activity assay Kit (ab65308, Abcam) was used to detect the cleavage of calpain substrate Ac-LLY-AFC. Sox2^{+} MB cells were counted and cultured on 5K polyacrylamide gel for at least 3 days, collected, pelleted by centrifugation, followed by being re-suspended in 100 μl extraction buffer and incubated on ice for 20 min. The tubes were tapped multiple times during incubation to achieve gentle mixing. After 1 min centrifugation with 10,000g, the cell lysate was diluted in 85 μl extraction buffer and transferred into 96-well plate. All inputs were standardized to same protein amount according to total protein measurement. 10 μl 10X reaction buffer and 5 μl calpain substrate were added to each assay well and incubated at 37 °C for 1 hour in dark. Measurements were carried out on a plate-reader with 400 nm excitation filter and 505 nm emission filter. The absorbance values after background subtraction are demonstrated as arbitrary units.

Western blotting

Total proteins of control and Piezo2 knockout Sox2^{+} MB cells, as well as MDA-MB-231 cells were extracted using a lysis buffer of 50 mM HEPES, 150 mM NaCl, 10% glycerol, 1 mM EDTA, and 1% NP-40, with protease inhibitors cocktail (Pierce^{TM} Prod# A32955) and 1 mM dithiothreitol (DTT). All lysates were kept on ice for 20 min, centrifuged 14,000 rpm at 4 °C for 10 min. Protein samples were resolved on 4-12% Bis-Tris gel (Invitrogen #NW04125BOX) at 200 V for 20 min with MES running buffer, transferred onto PVDF membrane (Millipore #IPVH0001), and blocked with 5% BSA and 0.1% Tween-20 in TBS. Western blotting were performed using primary antibodies diluted in the blocking solution. Immunoreactive bands were visualized using Bio-Rad Chemidoc imaging system. The primary antibodies used were: rabbit anti-SerpinB2 (ab137588, 1:1000) and mouse anti-αtubulin (Sigma Aldrich, 1:5000).

MALDI TOF MS imaging and LC-MS/MS

MALDI TOF MS imaging and LC-MS/MS were performed in MALDI MS Imaging Joint Facility and Mass Spectrometry Core Facility at Advanced Science Research Center of City University of New York (Veerasammy et al., 2020). High purity grade N(1-Naphthyl) Ethylenediamine Dihydrochloride (NEDC), 2,5-dihydroxybenzoic acid (DHB), Phosphorus (red), amino acid standards and SeQuant® ZIC-HILIC liquid chromatography 3.5 μm, 100 x 2.1 mm column were purchased from Millipore Sigma-Aldrich (USA). Optima UHPLC/MS-grade acetonitrile, ammonium acetate, methanol and water were purchased from Fisher Scientific (USA).

Mouse brains were harvested and snap frozen for 5 min on an aluminum boat floating on liquid nitrogen. The frozen tissue was cryosectioned at 10 μm thickness sections using CryoStar NX50 (Thermo Scientific, USA) at −15 °C set for both specimen head and the chamber. The tissue cryosections were gently transferred onto the pre-cooled conductive side of indium tin oxide (ITO)-coated glass slides (Bruker Daltonics, Bremen, Germany) for MALDI imaging. Mounted cryosections on ITO slides were desiccated in vacuum for 45 min at room temperature, followed by matrix deposition using HXT M5 sprayer (HXT LLC., USA). Matrix NEDC was used to detect amino acids (Wang et al., 2015), and a matrix solution of 10 mg/mL in methanol/water (70/30, v/v) was deposited at a flow rate of 0.1 ml/min and a nozzle temperature of 75 °C for 12 cycles with 5s drying between each cycle. Matrix DHB was used to detect drug etoposide, and a matrix solution of 40 mg/mL in methanol/water (70/30, v/v) was deposited at a flow rate of 0.12 ml/min and a nozzle temperature of 85 °C for 10 cycles. A spray velocity of 1300 mm/min, track spacing of 2 mm, N_2 gas pressure of 10 psi and flow rate of 3 L/min and nozzle height of 40 mm were used for both matrixes.

MALDI mass spectra were acquired in negative ion mode (for NEDC) or positive ion mode (for DHB) acquired by MALDI time-of-light (TOF) mass spectrometer Auto ex (Bruker Daltonics, Germany). MS spectra were calibrated using red phosphorus as the standard for all experiments. For etoposide experiment, the compound etoposide (1 mg/ml in 70% methanol) mixed with DHB matrix solution was also used as the reference. The laser spot diameters were focused to ''Medium'' modulated beam profile for 120 μm raster width. The imaging data for each array position were summed up by 500 shots at a laser repetition rate of 1000 Hz. To minimize broadening of ion peaks, we run all the experiments by setting laser power to its lowest value while it was still possible to accumulate ion spectra with appropriate S/N ratio. Spectra were acquired in the mass range from m/z 50 to 1000 with a low mass gate at 50 Da. Imaging data were recorded and processed using FlexImaging v3.0, and further analyzed using SCiLS. Ion images were generated with root-mean square (RMS) normalization and a bin width of ±0.10 Da. The spectra were interpreted manually, and analyte assignment was achieved by comparing with LC-MS experiment results and reference compounds loaded on the same MALDI slide. MALDI slides were retrieved immediately after the experiment, washed with 95% ethanol and proceeded with standard H&E staining. The H&E images were acquired using Leica Aperio CS2 slide scanner and used as anatomical reference for mass spectra imaging.

For LC-MS/MS, cold methanol method was used to extract metabolites (Ser et al., 2015). Briefly, tumor tissues were snap frozen in liquid nitrogen and approximate 40 mg of tissue was homogenized in 1ml cold Methanol/Water (80/20, v/v) stored at -20°C. Following 10 minutes of centrifugation at 4 °C, aliquots of 500 μl of the supernatants were dried using Speed-Vac and then resuspended in 150 μl of Acetonitrile/Water (90/10, v/v). 10 μl solution was subjected to LC-MS/MS experiments. Liquid chromatography-mass-spectrometry (LC-MS/MS) Global metabolic profiling was carried on all sample tissues using ZIC-HILIC chromatography (based on Acetonitrile/Water/2mM Ammonium acetate solvent systems) and high-resolution mass-spectrometry. We employed maXis-II-ETD UHR-ESI-Qq-TOF mass-spectrometer (Bruker Daltonics Inc., Germany) equipped with Dionex Ultimate-3000 liquid chromatography system ZIC-HILIC column operated at mildly acidic pH provided good performance on the metabolites of interest. Each LC-MS/MS experiment was performed in duplicate and statistical analysis of the acquired data was performed through XCMS software (Domingo-Almenara et al., 2018), which uses METLIN and Human Metabolome databases. Both mass-measurements (within 5 pmm accuracy) and fragmentation spectra (or simply MS/MS spectra) were used for identification of metabolites and etoposide.

Fluorescence in situ hybridization (FISH)

Cryosections were subjected to *in situ* hybridization with digoxigenin (DIG)-dUTP-labelled and fluorescein (FITC)-dUTP-labelled riboprobes for Piezo2 (F:GCGATTTAGGTGACACTATAGACAAGCACCCGGAACAGTAG, R:GCGTAATACGACTCACTATAGCCACCAGGTTCTGGCTGAAT) and Sox2 (https://mouse.brain-map.org/gene/show/20436). Probes were generated by PCR using mouse cerebellum cDNA as the template, followed by labelling using digoxigenin or fluorescein (Roche) with 200-300 ng of the PCR product. Double fluorescence in situ hybridization was performed as previously described (Hui and Joyner, 1993; Jandura et al., 2017). Briefly, sections were treated with proteinase K (10 mg/mL) for 15 minutes, 0.2 M HCl for 10 minutes, and 0.1 M triethanolamine with 0.25% acetic anhydride for 15 minutes. Hybridization with DIG- and FITC-labelled probes were conducted overnight at 55 °C. Slides were washed in saline-sodium citrate buffer and treated with 1% blocking reagent (Roche) prior to overnight incubation with anti-FITC-POD (1:500, Roche) at 4 °C, followed by tyramide signal amplification (TSA) with FITC-TSA (1:50, homemade) for 45 minutes at room temperature. For second probe development, slides were subsequently rinsed in 0.3% PBST, incubated with anti-DIG-POD (1:2000, Roche) overnight at 4 °C, and treated with Cy3-TSA (1:100, homemade) for 30 minutes at room temperature. Images were acquired using Leica SP8 confocal microscope and analyzed using Imaris and ImageJ. Cells containing signal puncta within or at the periphery of nucleus marked by DAPI were determined positive with transcript expression.

Single-cell RNA sequencing (scRNA-seq) and analysis

Sample preparation and scRNA-seq

Three *Math1-Cre; SmoM2* MBs and three *Math1-Cre; SmoM2; Piezo2$^{fl/fl}$* MBs from P21 mice were harvested followed by mechanical and enzymatic dissociation using the Papain Dissociation System (Worthington Biochemical Corporation). Single cell suspension was assessed by Trypan blue. Approximately 5,000 cells at a concentration of ~1,000 cells/μl were loaded onto the Chromium Controller. Library generation for 10X Genomics v3 chemistry was performed using the Chromium Single Cell 3' Reagents Kit. Quantifications of cDNA libraries were performed using the Kapa Library Quantification Illumina/ABI Prism Kit (KAPA Biosystems) and high-sensitivity DNA chips. 10X libraries were sequenced using the Illumina 2500 sequencing platform to achieve ~25,000 reads per cell.

Pre-processing of mouse scRNA-seq dataset

The Illumina sequencer's base call files (BCls) were demultiplexed into FASTQ files using *cellranger mkfastq*. The FASTQ files were aligned to GRCm38 (mm10) mouse genome reference to generate barcode-labeled sparse matrices individually by *cellranger count*. To identify expression dynamics of mRNAs, the outputs of *cellranger* were passed to *Velocyto run10x* pipeline. The aligned.loom files, containing qualified "unspliced", "spliced" and "ambiguous" molecules, were imported by *SeurateWrappers* package.

Processing of published human MB scRNA-seq datasets

We obtained scRNA-seq datasets of Human MB from previous studies from Gene Expression Omnibus (GEO; https://www.ncbi.nlm.nih.gov/geo/) (GEO: GSE119926 and GEO: GSE156053). The subgroups of medulloblastoma samples were classified based on DNA methylation. The transcriptomes of individual cells in scRNA-seq were from a plate-based full-length Smart-seq2 platform (GEO: GSE119926) (Hovestadt et al., 2019) or a droplet-based 10× Genomics platform (GEO: GSE156053) (Riemondy et al., 2022). We performed quality control and filtering using the same parameters as previous studies. After quality control and filtering, a total of 8,691 (Smart-seq2) and 39,946 (10× scRNA-seq) transcriptomes of single cells were obtained. The annotations of cell types in scRNA-seq datasets were provided by the authors in supplementary information. Data normalization was performed by *NormalizeData()* with "LogNormalize" method. Top 2,000 highly variable feature genes were selected by *FindVariableFeatures()* for principle component analysis. The significant PCs were used for Uniform Manifold Approximation and Projection (UMAP) to reduce to 2 dimensions by *RunMAP()* function. *PIEZO2$^+$; SOX2$^+$; GFAP$^+$* cells from scRNA-seq datasets were identified as cells that express all three genes.

Clustering, cell type identification, and differentially expressed gene analysis

The pre-processed barcode-labeled sparse matrices were passed to *Seurat v4.0* for data filtering (Stuart et al., 2019). Cells with high mitochondria gene percentage (percent.mt > 10%) and unique feature counts (nFeatures < 200 & nFeatures > 7,000) were filtered. Data normalization was performed by *NormalizeData()* with "LogNormalize" method. Top 2,000 highly variable feature genes were selected by *FindVariableFeatures()* for principle component analysis. We integrated single cell RNAseq datasets by following the tutorial of *Seurat v4.0*. The anchors were identified by *FindIntegrationAnchors()* and the datasets were integrated by *IntegrateData()*. For integrated dataset, significant principal components (PCs) dimensionalities were identified by ElbowPlot method. The significant PCs were used for Uniform Manifold Approximation and Projection (UMAP) to reduce to 2 dimensions by *RunMAP()* function. Cell clustering were generated by *FindNeighbors()* and *FindCluster()* functions. Marker genes of each cluster were determined by *FindAllMarkers()* with "roc" test, min.pct at 0.25 and logfc.threshold at 0.5. We categorized MB cells into six subgroups according to gene expression pattern of each cluster. Non-tumoral cell types were identified by referring to the *CellMarker* database (Zhang et al., 2019b). Differentially expressed genes between *Math1-Cre; SmoM2* and *Math1-Cre; SmoM2; Piezo2$^{fl/fl}$* MB were identified by *DESeq2*, and genes with q value < 0.1 were accepted as significant (Van den Berge et al., 2018). For Gene Set Enrichment Analysis (GSEA), genes were ranked according to $\log_2$ fold change from *DESeq2* output and processed to *GSEA()* from *clusterProfiler* R package.

Single-cell enrichment analysis

We generated gene signatures of SHH MB by referencing to human MB (Hovestadt et al., 2019) and published Cell Cycle gene signatures (Mizuno et al., 2009). We utilized *AUCell* from *SCENIC* pipeline to generate single cell gene set enrichment scores. Enrichment scores of SHH-A, SHH-B and SHH-C gene signatures were used to identify SHH MB subgroups. G1 enrichment score from AUCell was used for G0-G1 trajectory pseudotime validation.

Cell cycle identification and G0-G1 pseudotime reconstruction of Sox2$^+$ MB cells

Sox2$^+$ MB cells were identified using *WhichCells()* from *Seurat* R package. These cells were re-normalized, re-clustered and re-scaled by standard *Seurat* procedures. The UMAP of Sox2$^+$ MB cells was conducted by selecting top 7 reduced PCA dimensions. Cell cycle phases of Sox2$^+$ MB cells were identified by *CellCycleScoring()*. Less cycling cells assigned into G1 phase were identified as G0/G1 Sox2$^+$ MB cells. To identify G0-like and G1-like Sox2$^+$ MB cells, we re-ran PCA on those G0/G1 Sox2$^+$ MB cells. The G0/G1 Sox2$^+$ MB cells were re-clustered by *FindNeighbors()* and *FindCluster()* functions. Marker genes of clusters were identified by *FindAllMarkers()*. We used *dyno* pipeline for G0-G1 pseudotime reconstruction (Saelens et al., 2019). Expression matrix was transformed by *wrap_expression()* from Seurat object. The G0-G1 trajectory was inferred by *infer_trajectorires()*.To reconstruct a linear like trajectory, TSCAN was selected from *dyno* pipeline (Ji and Ji, 2016). The TSCAN-generated G0-G1 pseudotime were confirmed by marker genes and G1 enrichment score. To compare the G0-G1 pseudotime progression between Sox2$^+$ MB cells of *Math1-Cre; SmoM2* and *Math1-Cre; SmoM2; Piezo2$^{fl/fl}$* mice, Wilcoxon Rank Sum Test was performed.

RNA velocity of Sox2$^+$ MB cells

We analyzed RNA velocity of Sox2$^+$ MB cells by *velocyto.R* and *SeuratWrappers* packages (La Manno et al., 2018). Seurat objects with RNA velocity quantifications were generated by *WhichCells()*. We re-normalized the matrices and selected top 2,000 highly variable feature genes for PCA. The PC dimensionalities for cell clustering and UMAP plotting were identified by ElbowPlot. Cells were embedded into the UMAP plot. mRNA velocity were estimated using gene-relative model via *RunVelocity()*, which passed parameters to *gene.relative.velocity.estimates()*. We combined cell *k* nearest neighbors (kNN) pooling with gamma fit with min/max quantile fit at 0.02. The number of kNN in slope calculation smoothing was set at 7. Minimum average expression count for spliced and unspliced expression matrices were set as default at 0.2 and 0.05. We visualized mRNA velocity in UMAP embedding by *show.velocity.on.embedding.cor()*.

Patient cohort and survival analysis

RNA-seq or microarray data from human SHH MB were downloaded from a published source (EGA: EGAD00001001899, EGA: EGAD00001004958, and GEO: GSE85218). Raw counts were normalized using VST normalization (DESeq2). We selected patients under 17 years old as they were all subjected to the chemotherapy. Three tiers of *PIEZO2* expression (high, intermediate, low) were calculated using *k*-nearest neighbours ($k = 3$). Patient survival was correlated to *PIEZO2* expression and plotted using Kaplan-Meier curve. Statistical significance was determined using log-rank test.

By considering *PIEZO2* expression as continuous data, COX regression analysis was performed to determine association between *PIEZO2* expression and patient outcomes. The COX regression of *PIEZO2* expression in continuous value was fitted by *coxph()*.

Lentivirus production

CRYO-preserved HEK293T cells were thawed for culturing at least a week before experiments. One day before transfection, HEK293T cells were seeded at around 70% confluency. To produce lentivirus, 15 μg of lentiviral vectors, 10 μg of Gag-pol, Rev, Tat expression plasmids, and 5 μg of VSV-G expression plasmids were transfected into HEK293T cells cultured in 75 mm^2 flasks. 8 hours after transfection, the media was replaced with DMEM media containing 10% FBS and 1X NEAA (Thermo Fisher). 48 hours after media replacement, virus-containing media were collected and centrifuged at 4°C for 2 hours at the speed of 25,000 rpm. The viral pellets were resuspended in ice-cold DPBS, aliquoted, and stored in -80°C.

Xenograft study

Human PLKO.1 lentiviral shRNA target gene set against *PIEZO2* and PLKO.1-TRC-control vector were obtained from Dharmacon. Virus infections were performed in antibiotics-free culture medium for 24 hours. PIEZO2 shRNA mature antisense sequences are: #1: TAATTGTAGCTCTTGGTGAGG; #2: TTTCAACTGGCTTTGTTGGGC. 8-week old female *NOD scid gamma/J#5557* immunodeficient mice were used for xenograft experiments. Mice were housed under aseptic conditions, including filtered air and sterilized food, water, bedding, and cages. Mice were randomly assigned to experimental groups. The xenograft procedures were carried as previously described (Francisco et al., 2020). Briefly, mice were anesthetized using gaseous isoflurane and immobilized in a stereotaxic head frame. The skull of the mouse was then exposed, and a small opening was made using a sterile dental drill (Precision Guide) at 2 mm lateral and 3 mm posterior to lambda. At this location, 20,000 ONS76 with non-targeting shRNA or PIEZO2 shRNA in 2μl culture media were slowly injected (over 2min) 2 mm deep to the surface of the skull using a 26G Hamilton syringe. All procedures were performed under sterile conditions. Tumor cells were transduced with firefly luciferase-expressing reporter and tumor growth in mice was monitored through *in vivo* bioluminescence imaging using Xenogen IVIS Lumina System coupled to LivingImage software for data acquisition. Time-matched tumors were collected and processed for immunohistochemistry and TEM.

BTB permeability assay

Math1-Cre; SmoM2 and *Math1-Cre; SmoM2; Piezo2$^{fl/fl}$* P21 MB-bearing mice or mice bearing ONS76 xenograft tumors were anaesthetized. Cadaverine-Alexa555 (12.5 μg/g body weight, A30677, Invitrogen), Dextran-Alexa555 (12.5 μg/g body weight, D34679, Invitrogen) or Evans blue (2% in saline, 3 mL/kg body weight, E2129, Sigma Aldrich) was injected into the retro-orbital sinus. After two hours, the mice were anaesthetized and perfused with PBS followed by 4% paraformaldehyde. The brains were dissected and post-fixed overnight at 4°C before cryosection. Tracers in tumors was determined by Leica SP8 confocal microscope.

Computational simulation of mechanical stress within the BTB

Model geometry

A computational model was developed using COMSOL Multiphysics 5.4 to simulate the transmission and distribution of pericyte-generated force within the BTB (Wang et al., 2018). The multi-layer model, which is composed of Sox2^{+} MB cell endfeet, pericyte, basement membrane, and endothelial cell, is reconstructed based on transmission electron microscopy images of the BTB. The default mesh size was set as 0.458 nm.

Boundary condition

A zero-displacement boundary condition was imposed at the bottom of endothelial cells. Adjacent layers were assigned as inseparable. Blood within the capillary lumen was assigned to be freely moving liquid.

Mechanical properties

The mechanical properties of each layer were set as isotropic elastic with Young's modulus of 0.5 kPa for Sox2^{+} MB cell endfeet, 0.5 kPa for pericyte, 20 kPa for basement membrane (Reuten et al., 2021), and 3 kPa for endothelial cell (Byfield et al., 2009).

Applied load

The mechanical force generated by pericyte was applied to pericyte's edge, mimicking the force generated near pericyte processes onto the basement membrane and endothelial cells (Dessalles et al., 2021). The force generated by the pericyte was assigned to be 7 nN for the control group and 1.55 nN for the Piezo2 knockout group. The force was calculated based on the quantification results from traction force microscopy and phosphorylated myosin light chain II staining. A counterbalance force was applied globally on the surface of the structure.

When applying an external load to the multi-layer structure, a spherical indenter with a radius of 1.5 μm was included on top of the multi-layered BTB model. The force of 10 pN was applied perpendicular to the contact surface, and the stress distribution was then studied within the BTB.

Self-consistency of the computation model

Mesh sensitivity was investigated to ensure independence of the results from the computational mesh size. Three mesh sizes were used. "Fine", "Finer" and "Extra Fine" (defined by COMSOL) meshes with mesh size of 0.458 nm, 0.287 nm, and 0.110 nm were used for comparison. The solution patterns did not depend on patterns of the mesh lines. The maximum differences between three computational meshes were less than 1% for maximum stress in the basement membrane. The results proved self-consistency of the computation model.

QUANTIFICATION AND STATISTICAL ANALYSIS

No statistical methods were used to pre-determine sample sizes. The statistical analyses were done afterwards without interim data analysis. No data points were excluded. Two-tailed Student's t-test was performed for comparison between two groups of samples. One-way ANOVA with Tukey's multiple comparisons correction or Kruskal-Wallis test with Dunn's multiple comparisons correction were used to analyse differences between multiple groups. Two-way ANOVA analyses with Geisser-Greenhouse correction were used to assess significance of multiple data points. The Kaplan–Meier estimator and GraphPad Prism software were used to generate survival curves. Differences between survival curves were calculated using a log-rank test. All data were collected and processed randomly. Each experiment was reproduced at least three times and was performed on different days. All measurements were taken from distinct samples. All data are expressed as mean ± s.e.m. *P* value less than 0.05 is considered statistically significant. The statistical details of experiments, the exact values of *n* and what they represent can be found in the figure legends.